frontiers in Ecology and Evolution

ORIGINAL RESEARCH
published: 28 March 2022
doi: 10.3389/fevo.2022.853404

Volcanically-Induced Environmental and Floral Changes Across the Triassic-Jurassic (T-J) Transition

Peixin Zhang[1], Jing Lu[1], Minfang Yang[2], David P. G. Bond[3], Sarah E. Greene[4], Le Liu[1], Yuanfu Zhang[5], Ye Wang[1], Ziwei Wang[1], Shan Li[1], Longyi Shao[1] and Jason Hilton[4]**

[1] State Key Laboratory of Coal Resources and Safe Mining, College of Geoscience and Surveying Engineering, China University of Mining and Technology, Beijing, China, [2] Research Institute of Petroleum Exploration and Development, PetroChina, Beijing, China, [3] Department of Geography, Geology and Environment, University of Hull, Hull, United Kingdom, [4] School of Geography, Earth and Environmental Sciences, University of Birmingham, Birmingham, United Kingdom, [5] School of Energy Resources, China University of Geosciences, Beijing, China

The End-Triassic Mass Extinction (ETME) saw the catastrophic loss of *ca.* 50% of marine genera temporally associated with emplacement of the Central Atlantic Magmatic Province (CAMP). However, the effects of the ETME on land is a controversial topic. Evaluation of the disparate cause(s) and effects of the extinction requires additional, detailed terrestrial records of these events. Here, we present a multidisciplinary record of volcanism and environmental change from an expanded Triassic-Jurassic (T-J) transition preserved in lacustrine sediments from the Jiyuan Basin, North China. High-resolution chemostratigraphy, palynological, kerogen, and sedimentological data reveal that terrestrial conditions responded to and were defined by large-scale volcanism. The record of sedimentary mercury reveals two discrete CAMP eruptive phases during the T-J transition. Each of these can be correlated with large, negative C isotope excursions (CIE-I of −4.7‰; CIE-II of −2.9‰), significantly reduced plant diversity (with *ca.* 45 and 44% generic losses, respectively), enhanced wildfire (marked by increased fusinite or charcoal content), and major climatic shifts toward drier and hotter conditions (indicated by the occurrence of calcareous nodules, increased *Classopollis* pollen content, and PCA analysis). Our results show that CAMP eruptions may have followed a bimodal eruptive model and demonstrate the powerful ability of large-scale volcanism to alter the global C cycle and profoundly affect the climate, in turn leading to enhanced wildfires and a collapse in land plant diversity during the T-J transition.

Keywords: End-Triassic Mass Extinction, palynology, volcanism, paleoenvironment, paleoclimate, carbon cycle, North China

OPEN ACCESS

Edited by:
Sara Callegaro, University of Oslo, Norway

Reviewed by:
Simonetta Cirilli, University of Perugia, Italy
Guillaume Paris, UMR 7358 Centre de Recherches Pétrographiques et Géochimiques (CRPG), France

***Correspondence:**
Jing Lu
lujing@cumtb.edu.cn
Jason Hilton
J.M.Hilton@bham.ac.uk

Specialty section:
This article was submitted to Paleontology, a section of the journal Frontiers in Ecology and Evolution

Received: *12 January 2022*
Accepted: *24 February 2022*
Published: *28 March 2022*

Citation:
Zhang P, Lu J, Yang M, Bond DPG, Greene SE, Liu L, Zhang Y, Wang Y, Wang Z, Li S, Shao L and Hilton J (2022) Volcanically-Induced Environmental and Floral Changes Across the Triassic-Jurassic (T-J) Transition. Front. Ecol. Evol. 10:853404. doi: 10.3389/fevo.2022.853404

INTRODUCTION

As one of the five biggest Phanerozoic extinctions in Earth history, the End-Triassic Mass Extinction (ETME, *ca.* 201.51 Ma) during the Triassic-Jurassic (T-J) transition resulted in the loss of *ca.* 50% of marine genera (Raup and Sepkoski, 1982; Dal Corso et al., 2014; Miller and Baranyi, 2021). However, the impact of this crisis on terrestrial plant diversity is poorly understood. Studies of plant macrofossils and palynological (spore-pollen) assemblages reveal that plant diversity and many dominant species suffered severe losses in the Tethys ocean domain of the northern

hemisphere in Europe (McElwain et al., 1999, 2007; Kuerschner et al., 2007; Bonis et al., 2009, 2010; Pieńkowski et al., 2012; Lindström, 2016, 2021; Lindström et al., 2019; Wignall and Atkinson, 2020), North America (Olsen et al., 2002), South China (Wang et al., 2010; Li et al., 2020; Zhou et al., 2021), and northwest (NW) China (Lu and Deng, 2005; Deng et al., 2010; Sha et al., 2015; Fang et al., 2021). Similar losses are known from southern hemisphere Australia and New Zealand (De Jersey and McKellar, 2013). However, this is not completely supported by data from the Fundy Basin in North America (Marzoli et al., 2008; Cirilli et al., 2009; Cirilli, 2010) or southern Europe (Cirilli et al., 2015, 2018; Vilas-Boas et al., 2021) where low biodiversity losses are recorded across the T-J boundary (TJB). Similarly, recent studies from Poland and other western Tethyan locations found no significant changes in plant diversity and community succession through the T-J transition (Lucas and Tanner, 2015; Barbacka et al., 2017; Lucas, 2021). In Morocco, palynological assemblages record losses in the Rhaetian that suggest the terrestrial crisis was slightly older than the TJB (Panfili et al., 2019). Evaluation of the fate of terrestrial plants during the ETME requires further detailed records of floral diversity and associated environmental and climate changes from continental successions across different latitudes and climatic zones.

The Central Atlantic Magmatic Province (CAMP) is one of the most voluminous large igneous provinces (LIPs) on Earth and its emplacement was near-synchronous with the ETME (Schoene et al., 2010; Wotzlaw et al., 2014). The close temporal association between CAMP and the extinction losses has led to volcanism being implicated as a driver of the ETME (Bond and Wignall, 2014; Percival et al., 2017; Lindström et al., 2019; Panfili et al., 2019). The massive input of CAMP greenhouse gases (e.g., CO_2 and CH_4) into the atmosphere-ocean system would likely have driven rapid global warming (Hesselbo et al., 2002; Marzoli et al., 2004; Cirilli et al., 2009, 2015, 2018; Svensen et al., 2009; Dal Corso et al., 2014; Percival et al., 2017; Panfili et al., 2019; Heimdal et al., 2020; Ruhl et al., 2020; Capriolo et al., 2021a,b). Some studies from West Tethys and South China demonstrate wildfires associated with global warming played an important role for changes in terrestrial vegetation and ecosystems (Belcher et al., 2010; Petersen and Lindström, 2012; Lindström et al., 2019, 2021; Song et al., 2020), with enhanced wildfire leading to catastrophic soil erosion following vegetation loss (van de Schootbrugge et al., 2020; Lindström et al., 2021). However, it remains unknown whether wildfire during the T-J transition was localized or extended across the world as it appears to have done during the Permian-Triassic terrestrial mass extinction (e.g., Glasspool et al., 2015; Lu et al., 2020a; Dal Corso et al., 2022). As a result, further study is needed to enhance our understanding of the relationship between volcanic activity, wildfire, and terrestrial plant evolution across this key geological time interval.

We investigate a terrestrial succession from the Zuanjing-1 (ZJ-1) borehole in the Jiyuan Basin of the southern North China Plate (NCP). We use fossil plant biostratigraphy and organic C isotope ($\delta^{13}C_{org}$) chemostratigraphy together with Hg concentrations to correlate changes in plant composition and diversity with volcanic activity during the T-J transition.

GEOLOGICAL SETTING

During the Late Triassic, the NCP was located at approximately 30–40°N in the eastern Tethys Ocean (Greene et al., 2012; **Figures 1A,B**). The Yinshan paleoland lay to the north and the Qinling-Dabie Orogenic Belt (QDOB) to the south (Liu et al., 2013; **Figure 1B**). The Ordos Basin occupied the central and southwestern parts of the NCP and incorporated the smaller Jiyuan Basin at its southeast margin (Liu et al., 2013; **Figure 1B**). From the Late Triassic to the Jurassic the Jiyuan Basin was a lake (Li et al., 2014) that received sediment from the QDOB and southern NCP (Yang et al., 2012; **Figures 1A,B**).

The stratigraphic and lithologic succession and fossil plant assemblages from the Late Triassic to the Middle Jurassic of the Jiyuan Basin are shown in **Figure 1C**. The age of the Jiyuan succession is constrained by its flora and through zircon dating (see Lu et al., 2021a). The Tanzhuang Formation and the lower part of the Anyao Formation are considered to be Late Triassic in age based on the presence of the *Danaeopsis-Bernoullia* fossil plant assemblage (Hu, 1991; **Figure 1C**). Zircon U-Pb ages from two tuffaceous claystone horizons in the topmost part of the Tanzhuang Formation (233.1 ± 1.3 and 232.9 ± 2.1 Ma; Lu et al., 2021a) confirm this age assignment. The upper part of the Anyao Formation lacks biostratigraphically informative megafossils (Hu, 1991) but it can be assigned to the T-J transition based on its position between underlying Triassic strata and the overlying Jurassic-aged Yangshuzhuang Formation based on biostratigraphy and the presence of the *Coniopteris–Phoenicopsis* floral plant assemblage (Hu, 1991; **Figure 1C**).

MATERIALS AND METHODS

Fifty fresh mudstone drill core samples from the Anyao Formation were taken from the ZJ-1 borehole (35.07001°N, 112.47338°E) that was drilled in the Jiyuan Basin (**Figures 1A,B**; sampling locations are shown in **Figure 2**). These samples were analyzed for their geochemistry and palynology. Each sample was first divided into two parts of which one was crushed into particles *ca.* 1 mm in diameter for analysis of (1) kerogen enrichment and (2) palynological isolation. The remaining part of the sample was crushed to pass through a 200 μm mesh and then divided into seven subparts for analysis of (1) $\delta^{13}C_{org}$, (2) total organic carbon (TOC), (3) total nitrogen (TN), (4) mercury (Hg) content, (5) total sulfur (TS), (6) major elements, and (7) Rock-Eval pyrolysis.

Hg concentrations were measured at the State Key Laboratory of Coal Resources and Safe Mining (Beijing). $\delta^{13}C_{org}$, TS, and major elements were measured at the Beijing Research Institute of Uranium Geology, and TOC and TN were measured at the Research Institute of Petroleum Exploration and Development Research (RIPED). Hg concentration was undertaken using a mercury analyzer (Lumex RA-915 +) with lower detection limits of 2 ng/g (2 ppb). The mercury analyzer was calibrated before use with standards of China National Certified Reference Material soil (CRMs; GBW07427) with Hg concentration of 52 ± 6 ppb, and analytic precision was within 5%. $\delta^{13}C_{org}$ analysis was

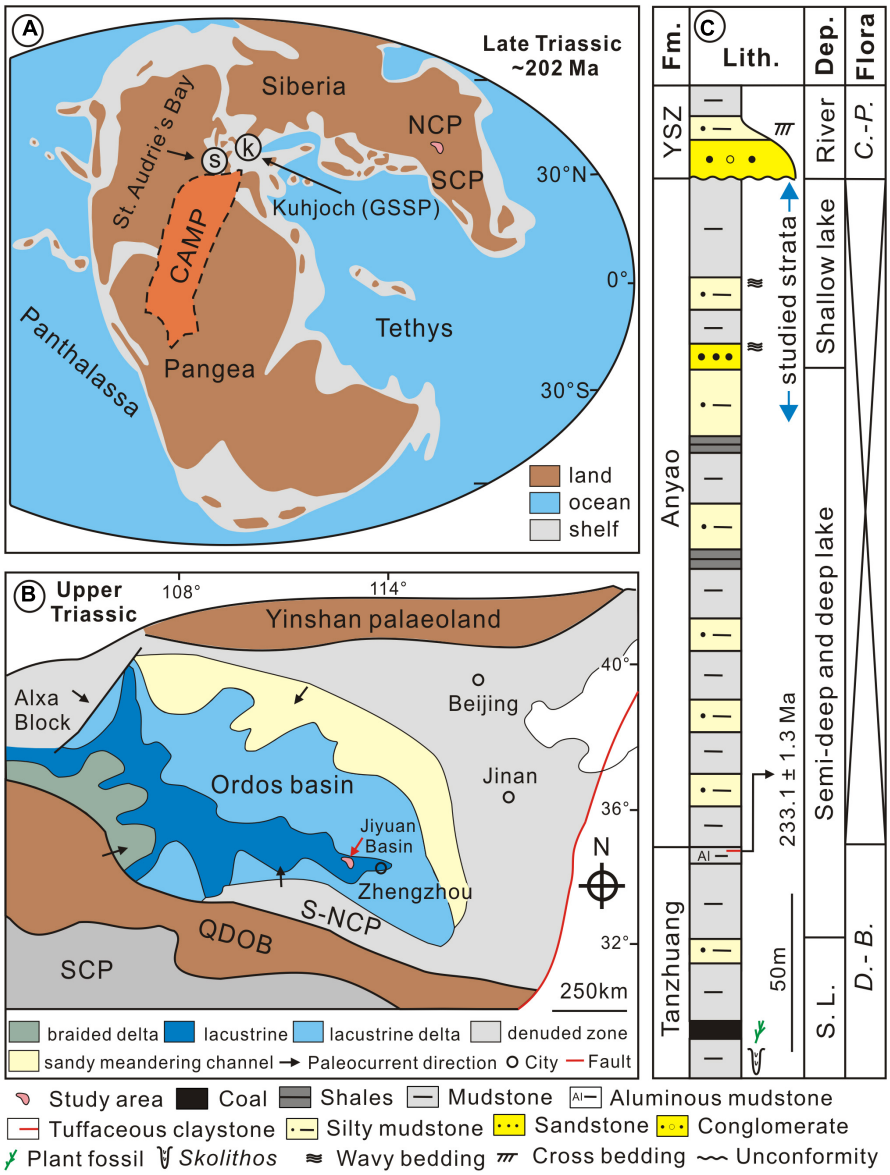

FIGURE 1 | Location and geological context for the study area. **(A)** Paleogeographic reconstruction for the Late Triassic (~202 Ma) showing the location of the NCP and approximate extent of CAMP (revised after Greene et al., 2012); **(B)** simplified tectonic map of the southern NCP during the Late Triassic showing the location of the study area (modified from Liu et al., 2013); **(C)** stratigraphic framework of the Tanzhuang Formation to the Lower Yangshuzhuang (YSZ) Formation from the Jiyuan Basin (modified from Yang et al., 2012). Depositional environments come from Li et al. (2014). Note that U-Pb dating (233.1 ± 1.3 Ma) come from Lu et al. (2021a). CAMP, Central Atlantic Magmatic Province; NCP, North China Plate; SCP, South China Plate; QDOB, Qinling-Dabie Orogenic Belt; S-NCP, southern North China Plate; Fm., Formation; Lith., Lithology; Dep., Depositional environment; *C.-P.*, *Coniopteris-Phoenicopsis*.

performed using a stable isotope mass spectrometer (MAT253), and $\delta^{13}C_{org}$ values are expressed in per mil (‰) with respect to the Vienna Pee Dee Belemnite (VPDB) standard, with an absolute analysis error of ± 0.1‰. TS analysis was performed using a carbon-sulfur analyzer (Eltra CS580-A) with the lower detection limits of 30 ppm, yielding an analytical accuracy within 5% of the reported values. Major elements analysis was undertaken with an X-ray fluorescence spectrometer (PW2404). The spectrometer was calibrated before use with standards of CRMs (GBW07427), and analytic precision was within 5%. TOC and TN analysis was performed using an elemental analyzer (Vario MICRO Cube). To quantify the analytical results of TOC and TN, a certified reference material (L-alanine) was used during the analysis, yielding an analytical accuracy of 1.5 and 2% of the reported values, respectively. The analytic precision or error of all samples is based on reproducibility and repeats of the standard sample and standard samples were run after every five sample analyses. Detailed descriptions of analytical methods and errors used are available following those of Lu et al. (2020a,b, 2021a,b).

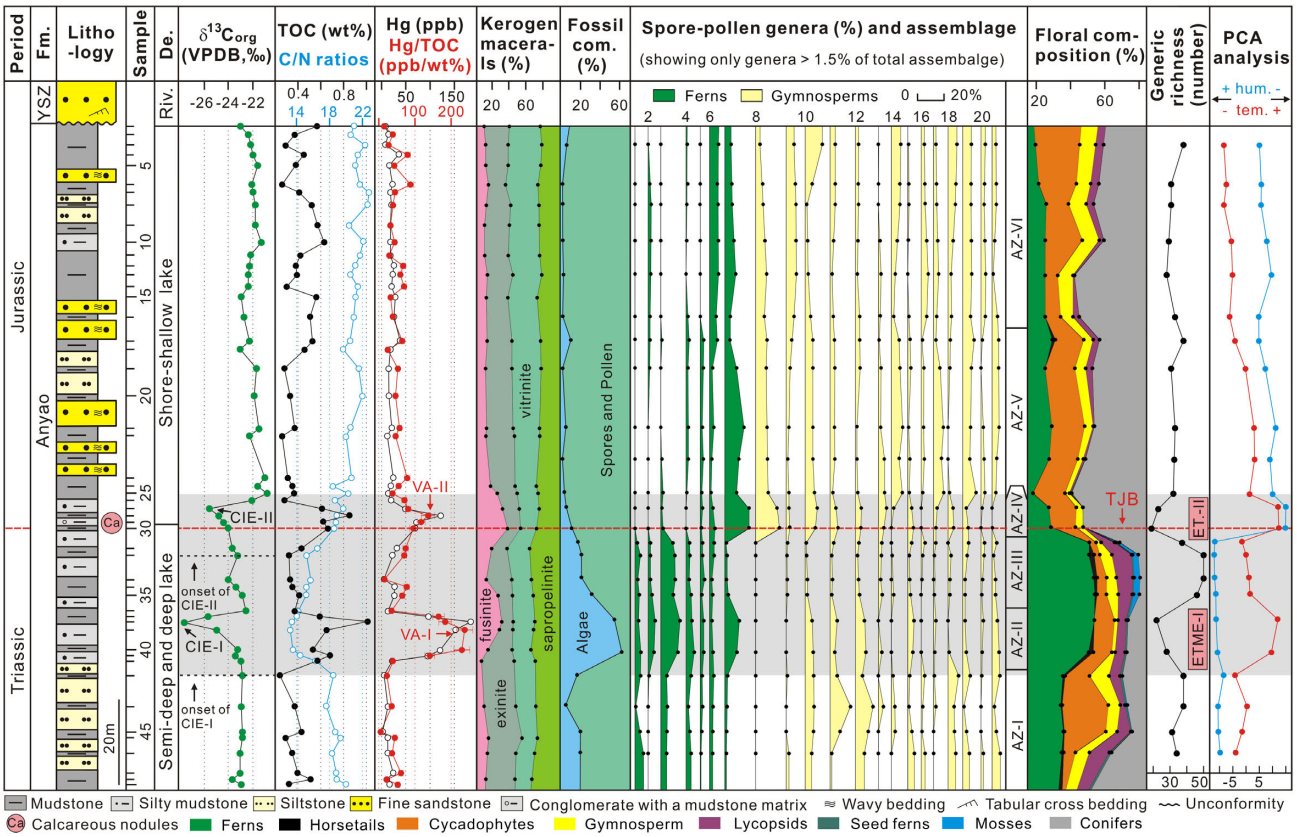

FIGURE 2 | Results of $\delta^{13}C_{org}$ values, TOC contents, C/N ratios, Hg concentrations, Hg/TOC ratios, kerogen macerals, fossil component, spore-pollen genera and palynology assemblage, floral composition, generic richness (number of different genera, excluding rework taxa), and principal components analysis (PCA) from the studied borehole in the Jiyuan Basin. Note that error bars on Hg/TOC plots represent the propagated error on Hg (± 5%) and TOC (± 0.2%) content measurements, and spore-pollen species more than 1.5% are plotted (more detailed data are shown in **Supplementary Table 1**). Fm., Formation; YSZ, Yangshuzhuang; De., Depositional environment; Riv., River; VPDB, Vienna Pee Dee Belemnite; CIE-I to CIE-II, from the first organic carbon isotope excursion to the second organic carbon isotope excursion; VA-I, first pulse of volcanic activity; VA-II, second pulse of volcanic activity; floral com., floral composition; 1, *Crassispora* (reworked); 2, *Triquitrites* (reworked); 3, *Anapiculatisporites*; 4, *Cyclogranisporites*; 5, *Dictyophyllidites*; 6, *Punctatisporites*; 7, *Leiotriletes*; 8, *Classopollis*; 9, *Cyathidites*; 10, *Pinuspollenites*; 11, *Osmundacidites*; 12, *Concentrisporites*; 13, *Cycadopites*; 14, *Chasmstosporites*; 15, *Psophosphaera*; 16, *Inaperturopollenites*; 17, *Vesicaspora*; 18, *Callialasporites*; 19, *Quadraeculina*; 20, *Rotundipollis*; 21, *Pseudopicea*; 22, *Protopinus*; 23, *Paleoconiferus*; AZ-I to AZ-VI, from the first palynology assemblage zone (AZ) I to the sixth palynology assemblage zone VI; TJB, Triassic-Jurassic boundary; ETME-I, the first stage of the end Triassic mass extinction; ET.-II, the second stage of the end Triassic mass extinction; PCA, principal component analysis; hum., humidity; tem., temperature.

Ten mudstone samples were selected for Rock-Eval pyrolysis at RIPED using an Oil and Gas Evaluation workstation (OEG-II) according to China National Standard (GB/T18602-2012). Kerogen enrichment and identification was performed on 30 of the 50 mudstone samples according to China national standard (SY/T5125–2014) at RIPED, with no less than 300 effective points per sample analyzed. Palynological isolation and identifications were undertaken for 23 of the 50 mudstone samples. Samples were subjected to acid digestion in 30% hydrochloric acid (HCl) and 38% hydrofluoric acid (HF). Heavy mineral separation was used to concentrate the sporomorphs and separate them from other components of the residue. For each spore-pollen sample, more than 100 sporomorphs were identified by the point-counting method under transmitted light microscopy (Olympus BX 41). All palynological slides are housed at the State Key Laboratory of Coal Resources and Safe Mining (Beijing). Percentages of spore and pollen taxa were calculated based on the sum of total sporomorphs. Palynological assemblages were identified by stratigraphically constrained cluster analysis (CONISS) using the Tilia software.

In this study, Hg concentration is used as a proxy for volcanism (e.g., Percival et al., 2017; Lu et al., 2020b, 2021a,b,c; Shen et al., 2020, 2022). Variations in spore-pollen composition through the studied strata were used to reconstruct paleoclimatic conditions (excluding reworked taxa, see **Supplementary Material**) based on the climatic preferences of the parent plants (e.g., Bonis et al., 2010; Lindström, 2016; Li et al., 2020; Lu et al., 2021a). Principal Components Analysis (PCA) by CANOCO software was performed to transform the relative abundances of spore-pollen (excluding reworked taxa, see **Supplementary Material**) into climatic parameters including temperature and humidity (e.g., Bonis et al., 2010; Li et al., 2020). Fusinite (charcoal) content is used as a proxy for paleo-wildfire activity (e.g., Glasspool et al., 2015; Lu et al., 2020a).

RESULTS AND ANALYSIS

Paleofloral Reconstruction and Paleoclimatological Inferences of Palynological Assemblages

From the samples 34 spore, 32 pollen, and 8 algae genera have been identified (**Supplementary Table 1**, **Figure 2**, and **Supplementary Figures 1, 2**) that are typical of Late Triassic and Early Jurassic palynological assemblages (see section "The Stratigraphic Position of the TJB in the Jiyuan Basin"). They are assigned to six palynological assemblage zones (AZ) based on the palynomorph abundance variations and CONISS: *Psophosphaera—Chasmatosporites—Cycadopites* assemblage zone (AZ–I; samples #JY 23—#JY 20), the *Punctatisporites—Cyathidites—Psophosphaera* assemblage zone (AZ–II, #JY 19—#JY 18), the *Punctatisporites—Verrucosisporites—Triquitrites* assemblage zone (AZ–III, #JY 17—#JY 14), the *Classopollis—Cyathidites—Cycadopites* assemblage zone (AZ–IV, #JY 13—#JY 12), the *Cyathidites—Classopollis—Pseudopicea* assemblage zone (AZ–V, #JY 11—#JY 7), and the *Pinuspollenites—Cycadopites—Classopollis* assemblage zone (AZ–VI, #JY 6—#JY 1) (**Figure 2** and **Supplementary Figure 1**). The composition of AZ-I is dominated by gymnosperm pollen (mean ($\bar{x}$) = 56.5%, including *Psophosphaera* and *Chasmstosporites*), followed by fern spores ($\bar{x}$ = 43.5%, including *Punctatisporites* and *Crassispora*). The compositions of AZ-II and AZ-III are noticeably different, although fern spores (including *Cyathidites* and *Punctatisporites*) dominate followed by gymnosperm pollen (including *Psophosphaera* and *Cycadopites*), but in AZ-II algae dominate ($\bar{x}$ = 57.6%) and the proportion of spores and pollens decreases by ca. 45% from 38 to 21 genera (**Figure 2**). Nine of the fern spore genera (dominated by *Verrucosisporites* and *Laevigatosporites*) and eight gymnosperm pollen genera (mainly *Rotundipollis*, *Podocarpidites* and *Callialasporites*) decreased in abundance (**Supplementary Table 1** and **Figure 2**). The compositions of AZ-IV, AZ-V, and AZ-VI are generally similar and are dominated by gymnosperm pollen ($\bar{x}$ = 72.0, 71.7, and 72.8%, respectively) including *Classopollis*, *Cycadopites,* and *Pseudopicea*. AZ-IV, AZ-V, and AZ-VI have low proportions of ferns ($\bar{x}$ = 28.0, 28.3, and 27.2%, respectively) including *Cyathidites* and *Osmundacidtes*, while algal composition is uniformly low ($\bar{x}$ = 7.1, 3.4, and 1.6%, respectively). In AZ-IV, the proportion of spores and pollens decreases by ca. 44% and from 50 to 28 genera. In this assemblage 14 fern spore genera (mainly *Verrucosisporites*, *Punctatisporites*, *Triquitrites,* and *Triporoletes*) and eight gymnosperm pollen genera (mainly *Paleoconiferus*, *Protopinus,* and *Callialasporites*) each decreased in abundance (**Supplementary Table 1** and **Figure 2**). In addition, AZ-IV (sample #JY 13) sees a decrease in diversity but a rapid increase in the abundance of *Classopollis* and *Cythidites*, and includes the first appearance of *Cerbropollenites* (**Figure 2**).

The parent plants of the palynological taxa have been evaluated to reconstruct the floral successions of the Jiyuan Basin (**Supplementary Tables 1, 2** and **Figure 2**). Diverse plant groups are recognized in the study area from the Late Triassic to Early Jurassic including mosses ($\bar{x}$ = 0.6%), lycopsids ($\bar{x}$ = 3.2%), horsetails ($\bar{x}$ = 0.7%), "filicalean" ferns ($\bar{x}$ = 34.0%), conifers ($\bar{x}$ = 39.9%), cycads ($\bar{x}$ = 14.7%), and pteridosperms (seed ferns; $\bar{x}$ = 0.4%) (**Supplementary Tables 1, 2** and **Figure 2**). These taxa mainly grow in temperate to subtropical, warm and humid climates (Liu et al., 2015; Li et al., 2020; Lu et al., 2021a). In AZ-I, AZ-II, and AZ-III, ferns are dominant ($\bar{x}$ = 34.8, 52.9, and 52.1%, including the Osmundaceae, Dicksoniaceae/Cyatheaceae, and Dipteridaceae/Matoniaceae), followed by conifers ($\bar{x}$ = 31.4, 28.8, and 24.1%, including Taxodiaceae and Podocarpaceae) and cycads. Horsetails and lycopsids are less abundant, while pteridosperms appear sporadically (**Supplementary Tables 1, 2**, **Figure 2**, and **Supplementary Figure 1**). In AZ-IV, AZ-V, and AZ-VI, conifers are dominant ($\bar{x}$ = 47.3, 49.4, and 47.3%, including Cheirolepidiaceae, Taxodiaceae, and Pinaceae), followed by ferns ($\bar{x}$ = 28.0, 25.9, and 23.8%, including Dicksoniaceae/Cyatheaceae and Osmundaceae), while cycads, horsetails, lycopsids, and seed ferns appear sporadically and mosses are absent (**Supplementary Tables 1, 2**, **Figure 2**, and **Supplementary Figure 1**).

Results of PCA analysis based on the relative abundance of spore-pollen genera are shown in **Figures 2–4**. Two main ordination axes representing the largest variance in palynological composition are used to explain the two most dominant environmental gradients that control the dataset (e.g., Bonis et al., 2010; Li et al., 2020). In this study, axis 1 and axis 2 separately account for 42.28 and 16.75% of the sporomorph spectra difference (**Figure 3**). On the positive side of axis 1, the xerophytic *Classopollis*, *Pinuspollenites,* and *Quadraeculina* pollen and hygro-mesophytic *Cyathidites* spores (e.g., Lindström, 2016; Li et al., 2020) have high scores, and the hygrophytic *Punctatisporites* spores (e.g., Lindström, 2016; Li et al., 2020) show high scores on the negative side of axis 1. Relatively cool, temperate conifer pollen including *Pinuspollenites* and *Pseudopicea* have high scores on the negative side of axis 2, and the relatively warm condition spores *Cyathidites* and *Punctatosporites* (e.g., Li et al., 2020) and the pollen *Classopollis* (e.g., Lindström, 2016) have high scores on the positive side of axis 2. Thus, the first and the second axes are interpreted to reflect the changes in relative humidity and temperature, respectively (**Figures 2**, **3**). The PCA results indicate stable cool-humid conditions prevailed during AZ-I, and cool-dry paleoclimate during AZ-V and AZ-VI, while mixed or fluctuating climatic conditions prevailed from AZ-II to AZ-IV, especially during two warming intervals in AZ-II and AZ-IV (**Figures 2**, **3**).

Total Organic Carbon and $\delta^{13}C_{org}$ Chemostratigraphy

Results for TOC and $\delta^{13}C_{org}$ are shown in **Figure 2** and **Supplementary Table 3**. TOC values vary from 0.24 to 1.01 wt% ($\bar{x}$ = 0.46 wt%). At the base of the succession TOC values are low and have a gradually decreasing trend in the mudstones and yellow siltstones (samples 50–43; $\bar{x}$ = 0.39 wt%), followed by an interval of fluctuating values and including two TOC peaks of 1.01 and 0.85 wt% in the latest Triassic-earliest Jurassic mudstones and gray siltstones (samples 42–25; $\bar{x}$ = 0.56 wt%). TOC values show a generally increasing

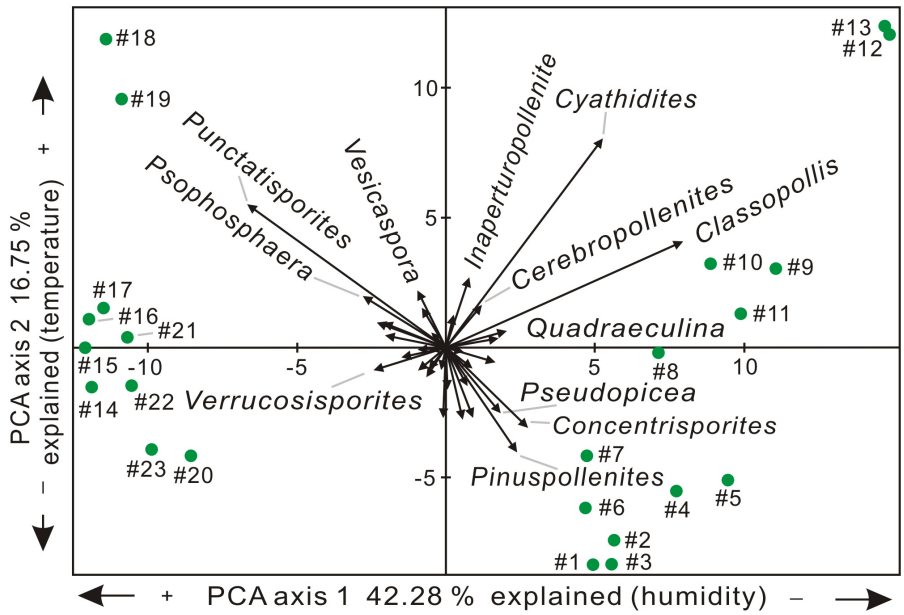

FIGURE 3 | Principal Component Analysis (PCA) ordination plot of sporomorph relative abundances (excluding reworked taxa) from the studied borehole in the Jiyuan Basin.

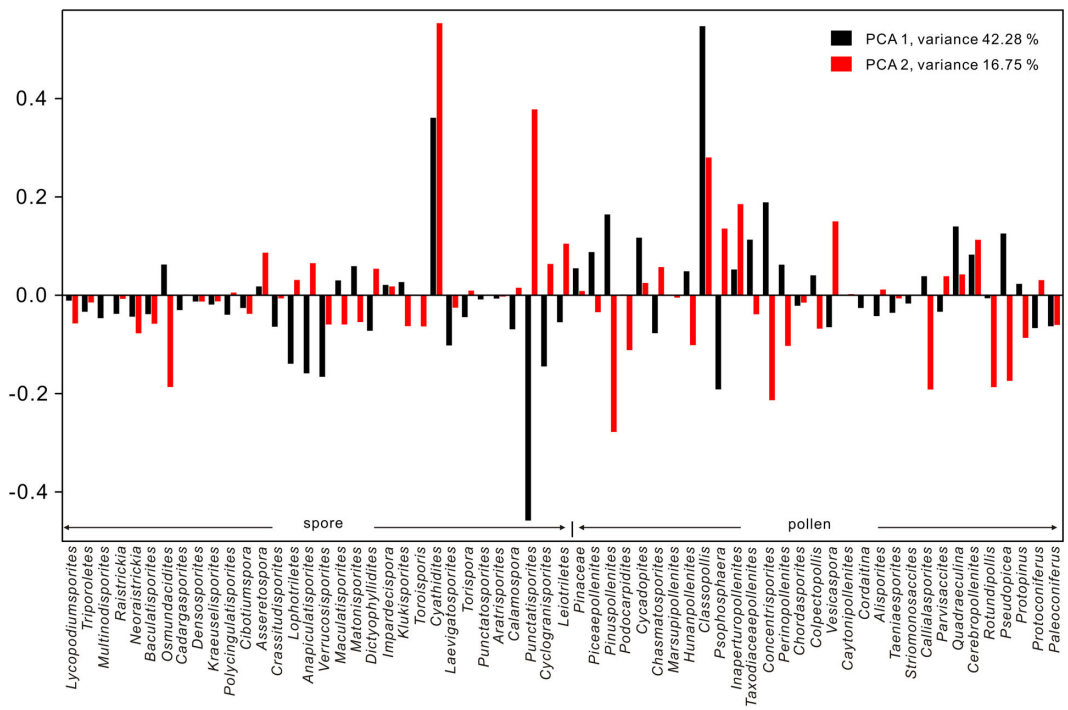

FIGURE 4 | Loading plots of PCA1 and PCA2 for spore and pollen genera (excluding rework taxa) from the studied borehole in the Jiyuan Basin.

trend through the Jurassic mudstones, siltstones, and sandstone to the top of our succession (samples 24–1; $\bar{x}$ = 0.44 wt%) (**Figure 2**). From samples through the complete succession, peak temperature of rock pyrolysis (T_{max}) values vary from 442 to 446°C ($\bar{x}$ = 444.1°C) (**Supplementary Table 3**) and indicate that kerogen maturity varies from low-maturity to mature as defined by the China National Standard (SY/T 5477-2003) (**Supplementary Table 5**).

$\delta^{13}C_{org}$ values vary from −27.5 to −20.8‰ ($\bar{x}$ = −22.8‰; **Figure 2**) and stratigraphically have two heavier plateaus either

side of a phase of lighter values around the T-J transition (**Figure 2**). In the earlier plateau (samples 50–43, roughly corresponding to AZ-I), $\delta^{13}C_{org}$ values are stable and average −22.9‰. In the phase of lighter values between the two plateaus (samples 42–25, roughly corresponding to AZ-II to AZ-IV) values vary from −29.0 to −22.5‰ ($\bar{x}$ = −24.3‰) and this part includes two negative $\delta^{13}C_{org}$ excursions (CIEs) with magnitudes of −4.7‰ (CIE-I) and −2.9‰ (CIE-II) relative to the background mean. These CIEs are near-synchronous with two falls in plant diversity in AZ-II and AZ-IV (**Figure 2**). Above CIE-II (samples 24–1, corresponding to AZ-V to AZ-VI), $\delta^{13}C_{org}$ values return to a heavier and stable plateau and average −22.0‰, including a slight decrease between samples 24 and 10 (**Figure 2**).

Kerogen Macerals as a Proxy for Wildfire

Kerogen macerals mainly comprise exinite ($\bar{x}$ = 29.1%), sapropelinite ($\bar{x}$ = 28.5%) and vitrinite ($\bar{x}$ = 26.4%), followed by fusinite ($\bar{x}$ = 16.1%) (**Supplementary Table 4** and **Figure 2**). Exinite content varies from 19.2 to 39.3% ($\bar{x}$ = 29.1%) and mainly comprises sporopollenite, cutinite, and subertinite (**Figures 2**, **5**). Sapropelinite content varies from 21.9 to 38.9% ($\bar{x}$ = 28.5%) (**Figures 2**, **5**). Vitrinite content varies from 12.4 to 37.8% ($\bar{x}$ = 26.4%) and comprises non-fluorescent telinite and collinite (**Figures 2**, **5**). Fusinite content varies from 6.7 to 39.6% ($\bar{x}$ = 16.1%) and is entirely fragmental fusinite which is opaque, pure black, does not fluoresce under fluorescence illumination, and is mostly long and thin or fragmental in shape with sharp edges (**Figures 2**, **5**). Fusinite enrichment in the studied strata (**Figure 2**) corresponds to the emergence of a large number of charcoal particles in sediments (**Figure 5**), with fusinite representing the product of incomplete combustion from wildfire (e.g., Goodarzi, 1985; Bustin and Guo, 1999; Lu et al., 2020a). We therefore use fusinite content as a proxy for wildfire. In this study, two obvious fusinite peaks with the values of 37.0 and 39.6% in the uppermost Triassic and earliest Jurassic strata (samples 38 and 30, respectively) correspond to the falls in plant diversity in AZ-II and AZ-IV (**Figure 2**).

Hg Anomalies as a Proxy for Volcanism

Results for Hg concentrations are shown in **Figure 2** and **Supplementary Table 3**. Hg concentrations show considerable variation, ranging from 2.23 to 183.42 ppb ($\bar{x}$ = 34.33 ppb) and have a distribution that is broadly anticorrelated to $\delta^{13}C_{org}$ values (**Figure 2**). The Hg concentrations show stronger covariation with TOC (r = + 0.67) than with Al (r = + 0.17) or TS (r = −0.03) (**Supplementary Figure 3**), suggesting Hg is mostly hosted by organic matter (OM) (e.g., Shen et al., 2020; Lu et al., 2021a,b,c). As a result, we present Hg/TOC values as a proxy for volcanism. Hg/TOC varies from 5.19 to 234.72 ppb/wt% ($\bar{x}$ = 66.16 ppb/wt%) with distribution broadly similar to the raw Hg concentrations (**Figure 2**). There are two Hg/TOC peaks with values of 234.72 ppb/wt% in AZ-II (from which we infer pulses of volcanic activity = VA-I) and 144.93 ppb/wt% in AZ-IV (VA-II; **Figure 2**). The intervals of Hg/TOC enrichment roughly correspond to the position of the CIEs, enhanced wildfire, and decreases in plant diversity (**Figure 2**).

DISCUSSION

The Stratigraphic Position of the T-J Boundary in the Jiyuan Basin

The TJB has been tentatively placed in the upper part of the Anyao Formation in the Jiyuan Basin (see Lu et al., 2021a and section "Geological Setting"). Palynological composition can be effective in determining stratigraphic age (e.g., Lu and Deng, 2005; Sha et al., 2015; Lindström et al., 2017; Li et al., 2020; Wignall and Atkinson, 2020). In western Tethys, floral changes near the TJB are characterized by: (1) an end-Triassic fern peak (including *Polypodiisporites polymicroforatus*, and trilete megaspores in some areas); (2) the earliest Jurassic first appearance (FO) of *Cerbropollenites thiergartii* and the last occurrence (LO) of *Lunatisporites rhaeticus*; and (3) a brief earliest Jurassic proliferation of *Classopollis* pollen (Cheirolepidiaceae) and the subsequent restoration and dominance of conifers (e.g., Olsen et al., 2002; Whiteside et al., 2007; Bonis et al., 2009, 2010; van de Schootbrugge et al., 2009; Pieńkowski et al., 2012; Vajda et al., 2013; Lindström et al., 2017; Wignall and Atkinson, 2020; Boomer et al., 2021). In eastern Tethys, a fern spore spike occurs in the Haojiaggou section from NW China during the T-J transition and is followed by the FO of *Cerbropollenites thiergartii*, the LO of *Lunatisporites rhaeticus*, and the co-dominance of *Classopollis* and *Cythidites* in Lower Jurassic strata (Lu and Deng, 2005; Deng et al., 2010; Sha et al., 2015; Fang et al., 2021); a fern spore spike also occurs in the Qilixia section of South China during T-J transition, followed by the co-dominance of *Classopollis* and *Cythidites* in the overlying Lower Jurassic strata (Wang et al., 2010; Li et al., 2020).

The combined records from the Haojiagou and Qilixia sections allow the development of an integrated stratigraphic TJB framework for the terrestrial eastern Tethys region (e.g., Lu and Deng, 2005; Li et al., 2020; Fang et al., 2021). In this study, similar changes in palynological assemblages allows us to correlate these two sections (see **Supplementary Material**). Significantly, the fern spore spike occurs in AZ-II and AZ-III in our study, but it lacks some of the usual fern elements including trilete type spores and *Polypodiisporites polymorphoratus*, which are key palynostratigraphic markers for the TJB in western Tethys (e.g., Lindström et al., 2017; Wignall and Atkinson, 2020). Similar patterns are also seen in the Haojiagou and Qilixia sections, which have been interpreted as the fern peak associated with global records from the T-J transition interval (see **Supplementary Material**). In our study, the spore and pollen composition of AZ-IV is very similar to that from the Badaowan Formation of NW China and the Zhenzhuchong Foamation of South China, with the co-dominance of *Cyathidites* (Dicksoniaceae/Cyatheaceae) and *Classopollis* (Cheirolepidiaceae), the common occurrence of *Cycadopites*, and the presence of *Dictyophyllidites*, *Chasmatosporites,* and *Quadraeculina*, which indicate an Early Jurassic age (e.g., Lu and Deng, 2005; Li et al., 2020). This is further supported by the disappearance at the base of AZ-IV of the Triassic taxa *Aratrisporites*, *Taeniaesporites*, and *Kraeuselisporites* (e.g., Fu and Yuan, 1998; Li et al., 2020). Furthermore, AZ-IV in the study

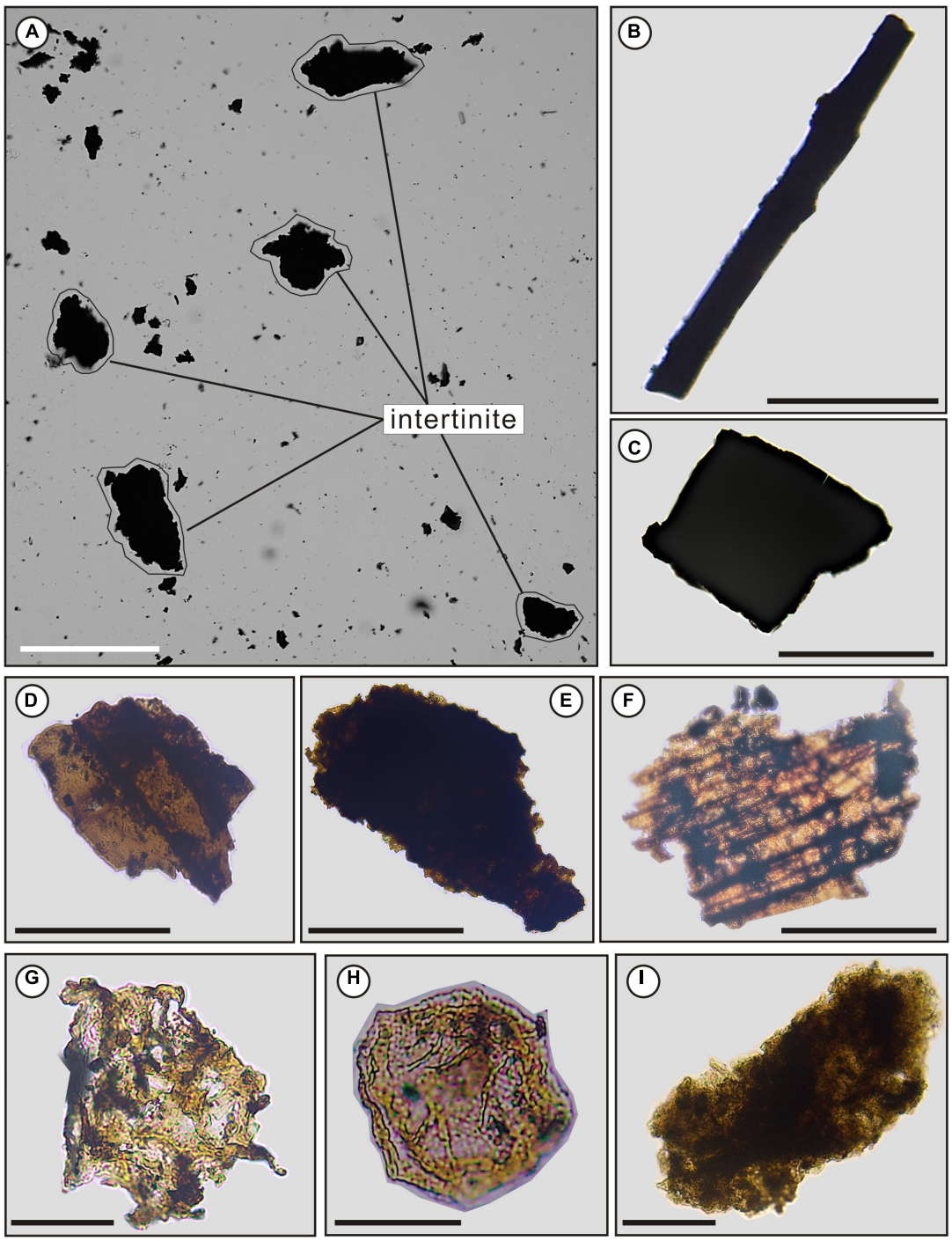

FIGURE 5 | Photomicrographs showing microstructure characteristics of kerogen macerals in the Jiyuan Basin (all scale bars = 50 μm). **(A)** Overview showing characteristics of inertinite (transmitted light, sample #38); **(B,C)** inertinite (transmitted light, samples #39 and #30); **(D,E)** vitrinite (transmitted light, sample #47); **(F)** suberinite (transmitted light, sample #19); **(G)** cutinite (transmitted light, sample #25); **(H)** saporopollenite (transmitted light, sample #42); **(I)** sapropelinite (transmitted light, sample #40).

area records the rapid proliferation of *Classopollis* pollen, and the subsequent restoration and dominance of conifers at the top of the assemblage zone (**Supplementary Table 1**, **Figure 2**, and **Supplementary Figure 1**). Similar records are known from the Early Jurassic of western Tethys (see above; e.g., Wignall and Atkinson, 2020). Collectively, these observations are consistent with the placement of the TJB at the base of AZ-IV (**Figure 2** and **Supplementary Figure 1**). As a result, we consider that the

fern spike recorded in the study area is representative of the global TJB record.

The T-J transition, beginning with the onset of the ETME, is one of the most ecologically significant intervals of the past 200 Ma and is characterized by dramatic global C cycle perturbations together with major changes in climate and ecosystem composition on land and in the oceans. Across the T-J transition, in particular where fossils or other diagnostic age markers are absent, chemostratigraphy and in particular C isotope stratigraphy can be used to correlate strata deposited in a diverse range of depositional environments (e.g., Korte et al., 2019; Pieńkowski et al., 2020; Ruhl et al., 2020; Fang et al., 2021).

In our study, Rock-Eval pyrolysis indicates that OM Rock-Eval pyrolysis data suggests that diagenetic processes are unlikely to be responsible for the observed shifts in the $\delta^{13}C$ signature of the OM, because such changes occur in late diagenetic to metamorphic burial stages that our material has not been subjected to (Dal Corso et al., 2018; Lu et al., 2021a). The two CIEs in the studied strata are also unlikely to have occurred through proportionate changes in terrestrial and algal organic carbon sources, which can be isotopically distinct from one another (Cloern et al., 2002). Variations in kerogen macerals reveal that the OM in the studied strata was from mixed sources of terrestrial plants and lacustrine plankton (see **Supplementary Material**). However, the proportion of OM sources did not change significantly during the two CIEs. Similarly, relatively high C/N ratios (see **Supplementary Material**) suggest that the OM throughout the succession is predominantly terrestrial with lower C/N ratios supporting a proportional increase in algal production during AZ-II and AZ-III (the shift to lower C/N ratios occurs between samples 42 and 41) (Cloern et al., 2002). Crucially no apparent relationship exists between C/N and $\delta^{13}C$ values across the CIEs. Furthermore, the $\delta^{13}C_{org}$ is largely limited by the pathway of plant photosynthesis and varies with plant types (e.g., Collister et al., 1994; Diefendorf and Freimuth, 2017). The two CIEs in the studied strata are synchronous with changes in fern spore and gymnosperm pollen abundances and the decreased plant diversity, indicating that whatever drove the CIEs might have affected the plant composition (e.g., van de Schootbrugge et al., 2008). However, changes in plant types is unlikely to be the driver of the observed CIEs in this study because those CIEs are remarkably similar to those in T-J transition $\delta^{13}C$ records in carbonates and in bulk marine and terrestrial OM (e.g., Bacon et al., 2011; **Figure 6** and **Supplementary Figure 4**). Compilation of global carbon isotope data has revealed a pattern of three isotopic excursions in both marine and continental strata. These comprise an initial excursion, then a small (unnamed) secondary excursion after a positive plateau, and finally a globally widespread main excursion (e.g., Hesselbo et al., 2002; Ruhl et al., 2009, 2010, 2020; Kovács et al., 2020; Wignall and Atkinson, 2020; Fang et al., 2021; Shen et al., 2022; **Figure 6**). In this study, the C isotope record exhibits similar features with two negative excursions comprising an initial CIE and an unnamed small CIE (**Figure 6**), that permit correlation with other TJB sections globally. The amplitude of the two CIEs in this study is consistent with those recorded in marine (–4 to –6.5‰) and continental (–2 to –4‰) strata in the Western Tethys Ocean in the middle and low latitudes of the northern hemisphere (**Figure 6** and **Supplementary Figure 4**). Therefore, we consider that CIE-I and CIE-II in this study reflect the changes to the global carbon cycle, namely the massive input carbon from an isotopically depleted carbon source.

In our study, CIE-I (−4.7‰) is characterized by a 45% reduction in plant diversity, the proliferation of fern spores, and an Hg/TOC peak (234.72 ppb/wt%, VA-I) during a phase of climatic warming (**Figures 2**, **6**). Similar features also characterize the former candidate global stratotype section and point (GSSP) at St. Audrie's section in the United Kingdom and the GSSP at Kuhjoch in Austria (**Figures 1A**, **6**). Here we use the candidate GSSP St. Audrie's section and the GSSP Kuhjoch section records as reference points (**Figures 1A**, **6**) since almost all other global T-J sections have been correlated with these (e.g., Ruhl et al., 2009, 2010, 2020; Lindström et al., 2017; Percival et al., 2017; Zaffani et al., 2018; Kovács et al., 2020; Pieńkowski et al., 2020; Wignall and Atkinson, 2020; Fang et al., 2021). However, numerous studies provide a range of interpretations in stratigraphic correlation, although in general the global C isotope curves are similar (Hesselbo et al., 2002; Ruhl et al., 2009, 2010, 2020; Lindström et al., 2017; Percival et al., 2017; Zaffani et al., 2018; Kovács et al., 2020; Wignall and Atkinson, 2020; Fang et al., 2021). The interpretation of Wignall and Atkinson (2020) is used here as it is the most representative and up to date. In their scheme, the initial CIE corresponds to the first extinction pulse that includes plant extinctions (see below) and Hg enrichment. A secondary unnamed CIE corresponds to a secondary extinction pulse that saw further losses within the plant record and Hg enrichment (e.g., Percival et al., 2017; Wignall and Atkinson, 2020). This indicates that the mass extinction history in Europe is pulsed and synchronous with C isotope excursions, facilitating global correlation of these phenomena (Wignall and Atkinson, 2020). Furthermore, the fern spore peaks in our study coincide with the initial CIE and the ETME. This observation has been reported in numerous sections (see references above) and further supports the placement of the onset of the ETME in the study area around CIE-I.

The younger CIE-II in the Jiyuan Basin succession is also widely known from marine and terrestrial records as the unnamed minor CIE in other areas (Hesselbo et al., 2002; Ruhl et al., 2009, 2010, 2020; Percival et al., 2017; Pieńkowski et al., 2020; Wignall and Atkinson, 2020; Fang et al., 2021; **Figure 6**). Like CIE-I, CIE-II is accompanied by a significant reduction in plant diversity in which 44% of genera are lost, and similar losses are known from other terrestrial records near the TJB (e.g., Wignall and Atkinson, 2020; Lindström, 2021). CIE-II is also accompanied by a minor Hg/TOC peak (144.93 ppb/wt%, VA-II). Warmer and drier climates persisted at this level in the study area indicated by the occurrence of calcareous nodules that formed through groundwater evaporation (e.g., Lu et al., 2020a and references therein) (**Figures 2**, **6**). Therefore, we consider it reasonable to place the TJB during the CIE-II interval based on (i) changes in biotic composition as reflected in biostratigraphy and palynofloral assemblage composition, and (ii) C isotope stratigraphy. This is supported by the ammonite-defined TJB at

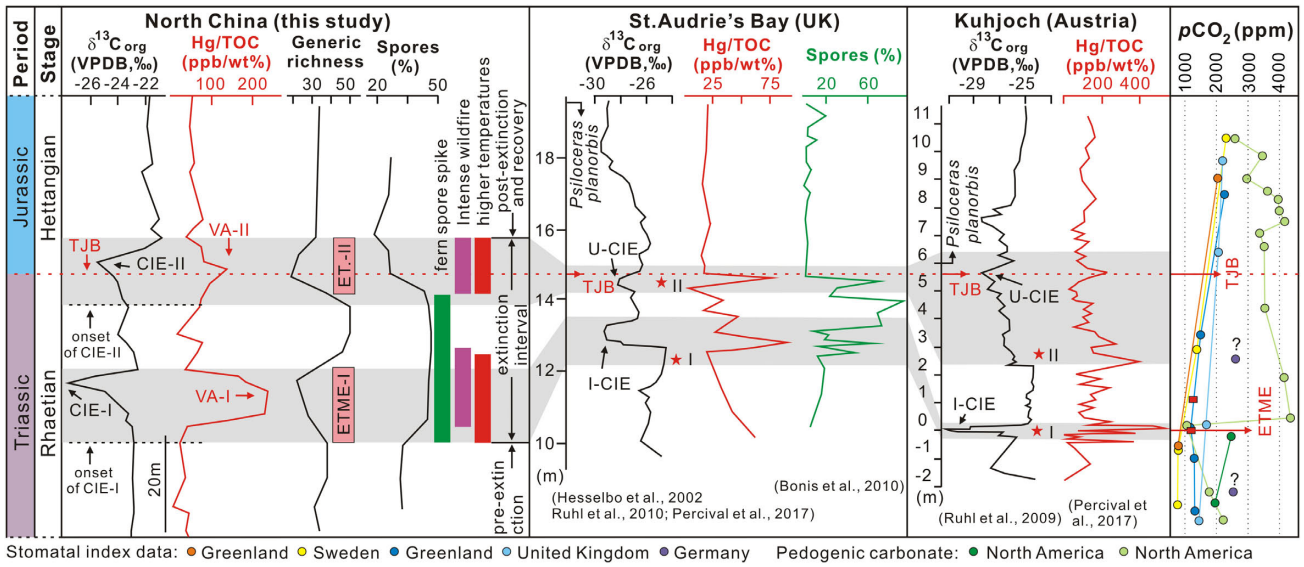

FIGURE 6 | Correlations of $\delta^{13}C_{org}$, Hg/TOC ratios, wildfire, spores (%), plant generic richness (number), and pCO_2 across the Triassic-Jurassic transition. Paleoclimate change inferred from palynology data. $\delta^{13}C_{org}$, Hg/TOC ratios, and spore data from the St. Audrie's Bay and Kuhjoch sections by Hesselbo et al. (2002), Ruhl et al. (2009), Bonis et al. (2010), Ruhl et al. (2010), and Percival et al. (2017) respectively; pCO_2 curves modified from Slodownik et al. (2021) and references therein. TJB, Triassic-Jurassic boundary; VPDB, Vienna Pee Dee Belemnite; CIE-I to CIE-II, from the first organic carbon isotope excursion to the second organic carbon isotope excursion; I-CIE, Initial CIE; U-CIE, Unnamed CIE; VA-I to VA-II, from the first volcanic activity to the second volcanic activity; ETME-I to ETME-II, from the first phase to the second phase of the end-Triassic mass extinction (ETME); Stars I and II mark the level of the first and second phase of extinction.

the GSSP at Kuhjoch, Austria (Ruhl et al., 2009) and other well-studied sections (e.g., Hesselbo et al., 2002; Percival et al., 2017; Pieńkowski et al., 2020; Ruhl et al., 2020; Wignall and Atkinson, 2020; Boomer et al., 2021; Fang et al., 2021; Shen et al., 2022) in which the TJB is below the main CIE and corresponds with a unnamed small negative CIE above the initial CIE (**Figure 6**).

Carbon cycle perturbations in the Jiyuan succession appear to have ended in the latter part of AZ-IV and the AZ-V interval is characterized by relatively stable C isotopic composition. This interval also saw stability return to climates and floral compositions (**Figures 2**, **6**), marking the end of the perturbations of the T-J transition. This can be correlated with records such as the Qilixia section in South China and the Haojiagou section in NW China, suggesting that the T-J transition approximately corresponds to the end of the secondary minor CIE, after the initial CIE (Fang et al., 2021; Shen et al., 2022).

Lacustrine Environmental and Floral Changes During the End-Triassic Mass Extinction

The timing and causal mechanism(s) of the ETME are controversial (e.g., van de Schootbrugge et al., 2009; Barbacka et al., 2017; Lindström et al., 2019; Wignall and Atkinson, 2020; Lindström, 2021; Lucas, 2021). Wignall and Atkinson (2020) document two pulses of extinction in marine and terrestrial settings, with pulses occurring during the initial and the minor (unnamed) negative CIEs during the T-J transition. On land, the first pulse of extinction is manifest as a decline in conifer pollen abundance and an overall plant diversity decline. This was followed by an interlude during which terrestrial assemblages were dominated by ferns, whose spores dominate the record from that interval. The second pulse of extinction caused another abrupt, palynological change, resulting in the loss of further pollen taxa and a brief proliferation of *Classopollis* pollen (Wignall and Atkinson, 2020). Our study also identifies a bimodal reduction in plant diversity, suggesting that the two-step extinction pattern is a globally widespread phenomenon (e.g., Wignall and Atkinson, 2020; Lindström, 2021). A rapid recovery of fern spores and their floral dominance (reaching 68.2% of all palynomorphs) (**Figure 2**) occurred in the interlude between ETME-I and ETME-II in the Jiyuan Basin. A similar pattern is known from both the southern and northern hemisphere including the Western Tethys ocean and the southern margins of Pangea (van de Schootbrugge et al., 2009; Lindström, 2016; Wignall and Atkinson, 2020).

The two pulses of plant diversity loss in the Jiyuan Basin (ETME-I and ETME-II) occurred during warming intervals indicated by the PCA analysis (**Figures 2**, **6**). Warming during the main CIE is supported by oxygen isotope data from oysters at Lavernock Point (United Kingdom) in the northwestern Tethys (Korte et al., 2009) and pCO_2 increases are recorded at both CIE levels are documented elsewhere in the record of pedogenic carbonates from the Newark Basin (Schaller et al., 2011) and the stomatal index (plant fossil cuticles) in Greenland and Sweden (McElwain et al., 1999; Slodownik et al., 2021), Germany (Bonis et al., 2010), and Northern Ireland (Steinthorsdottir et al., 2011; **Figure 6**).

Our data suggests that the two pulses of plant diversity collapse in the Jiyuan Basin are associated with significantly

different atmospheric humidities. ETME-I and the subsequent recovery occurred during humid conditions indicated by the proliferation of hygrophytic floral elements (including all spores, *Alisporites*, and *Cycadopites*) (**Figure 2** and **Supplementary Figure 1**). Similar records have been observed in Western Tethys (e.g., Hungary, Britain, Denmark, Greenland, and Canada) and southern Pangea (e.g., New Zealand, Western Australia, and Eastern Australia) and this has been interpreted as a result of increased humidity (van de Schootbrugge et al., 2009; Lindström, 2016). In contrast, ETME-II is associated with the development of an arid paleoclimate with high evaporation, as evidenced by decreased fern spore content, increasing Cheirolepidiaceae conifer content (*Classopollis* pollen), and the widespread occurrence of calcareous nodules in the core and in terrestrial outcrops (**Figures 2**, **7** and **Supplementary Figure 1**). Similar declines in fern spores and increases in gymnosperm pollen (e.g., *Classopollis* pollen) have been described for South China where they were interpreted as marking a shift toward warmer and drier conditions during the earliest Jurassic (Srivastava, 1976; Huang, 2001; Wang et al., 2010; Zhou et al., 2021).

In the Jiyuan Basin, ETME-I and ETME-II are also accompanied by enhanced paleo-wildfire indicated by the enrichment of fusinite (charcoal), as well as the appearance of a large number of charcoal particles in sediments (**Figures 3**, **7**). Enhanced wildfires during the T-J transition appears to be a global phenomenon (**Supplementary Figure 4**) as similar observations are known for other regions including North America (Jones et al., 2002), East Greenland (Belcher et al., 2010), Poland (Marynowski and Simoneit, 2009), Denmark and Sweden (Petersen and Lindström, 2012), and South China (Song et al., 2020).

A Volcanic Driver of Floral Change During the End-Triassic Mass Extinction

The emplacement of the CAMP is widely implicated as the ultimate driver of the ETME (Hesselbo et al., 2002; Schaltegger et al., 2008; Clémence et al., 2010; Bartolini et al., 2012; Percival et al., 2017; Lindström et al., 2019; Heimdal et al., 2020; Ruhl et al., 2020; Capriolo et al., 2021a,b; Shen et al., 2022). We have identified two Hg and Hg/TOC peaks in AZ-II and AZ-IV that are significantly higher than background levels seen in the other Assemblage Zones (**Figure 2** and **Supplementary Figure 5**). The behavior of Hg is complicated by depositional environment (Yager et al., 2021) and in terrestrial lake settings Hg can be sourced from the atmosphere (i.e., that associated with LIP volcanism) as well as from hydrological runoff (e.g., Shen et al., 2020; Lu et al., 2021a,b). The Hg preserved in the core material in this study is associated with OM derived from a mixture of terrestrial higher plants and lacustrine plankton in AZ-II and AZ-IV. Minor increases in TOC pre- and post-ETME are not accompanied by Hg peaks (**Figure 2**), supporting the notion that where terrestrial OM is enriched in Hg this was due to the effects of contemporaneous large-scale volcanism. Previous studies have shown that two or three Hg or Hg/TOC enrichment anomalies with likely origins in CAMP can be correlated across various sedimentary facies, from marine to terrestrial, during the T-J transition (Thibodeau et al., 2016; Percival et al., 2017; Lindström et al., 2019; Ruhl et al., 2020; Yager et al., 2021; Shen et al., 2022). Although the values of Hg and Hg/TOC enrichment anomalies vary spatially across different studied sections (**Figure 6**), Hg isotope data further support a CAMP source for elevated Hg contents across the ETME interval (Yager et al., 2021). Furthermore, two Hg enrichment anomalies in our study are synchronous with two pulses in terrestrial plant diversity, carbon cycle, enhanced wildfire and elevated temperature (**Figures 2**, **6**). Therefore, we consider the Hg/TOC ratios in this study as a reliable proxy for CAMP volcanism.

Volcanic activity can release copious amounts of isotopically light CO_2 into the reservoirs of the exogenic carbon cycle and can drive major global warming. As shown here and elsewhere (**Figure 6**), the close correspondence of Hg or Hg/TOC enrichment anomalies and CIEs during the T-J transition suggests that a large amount of isotopically light CO_2 entered the land atmosphere-ocean system during this interval. CLIMBER-3α + C Earth System model simulations suggest that pulses of CAMP volcanism potentially increased the global temperature by more than 4°C and might have triggered the disruption of the global end-Triassic carbon cycle (Landwehrs et al., 2020). Conservative estimates suggest that the emplacement of CAMP released between $\sim 1.4 \times 10^3$ Pg and 2.1×10^4 Pg of mantle C (Heimdal et al., 2020 and references therein). However, the isotope composition of volcanogenic CO_2 (mantle carbon $\sim -6‰$) means that the mass derived from CAMP emplacement is insufficient to drive the large negative CIEs associated with the ETME (e.g., Paris et al., 2016; Lindström et al., 2021). cGENIE model simulations (Vervoort et al., 2019) indicate that a negative CIE of $\geq 3‰$ (i.e., of similar magnitudes to those associated with the ETME), lasting ∼10–100 s of kyr, would require $> 3 \times 10^4$ PgC if the C mantle source had a $\delta^{13}C$ composition of $-6‰$. Similarly, GEOCLIM model simulations suggest that a CAMP-related negative CIE up to $\sim -6‰$ could be achieved by the release of repeated pulses of volcanic CO_2 if its isotopic signature was significantly light (–20‰; Paris et al., 2016). As a result, the ETME CIEs were likely in part driven by the addition of strongly ^{13}C-depleted C to the land atmosphere-ocean system from sources other than volcanic eruptions themselves. There is growing consensus that thermogenic C release was a contributing factor for the ETME CIEs (Svensen et al., 2009; van de Schootbrugge et al., 2009; Dal Corso et al., 2014; Heimdal et al., 2018, 2020). In addition, terrestrial or rock-bound organic C oxidation and methane release may have further contributed to the negative carbon isotope excursions (e.g., Ruhl et al., 2020; Capriolo et al., 2021a). In our study, two CIEs were contemporaneous with wildfires (**Figures 2**, **6**), raising the possibility that increased wildfire associated with volcanic activity provided a positive feedback in the global carbon cycle that further increased the magnitude of CIEs by releasing isotopically light carbon through combustion of biomass (e.g., Ivany and Salawitch, 1993; Belcher et al., 2010). Indeed, these hypotheses are not mutually exclusive and the different contributory factors probably acted in tandem to drive two major negative CIEs in the T-J interval. As a result, we favor a scenario in which repeated episodic light ^{13}C CO_2 release related

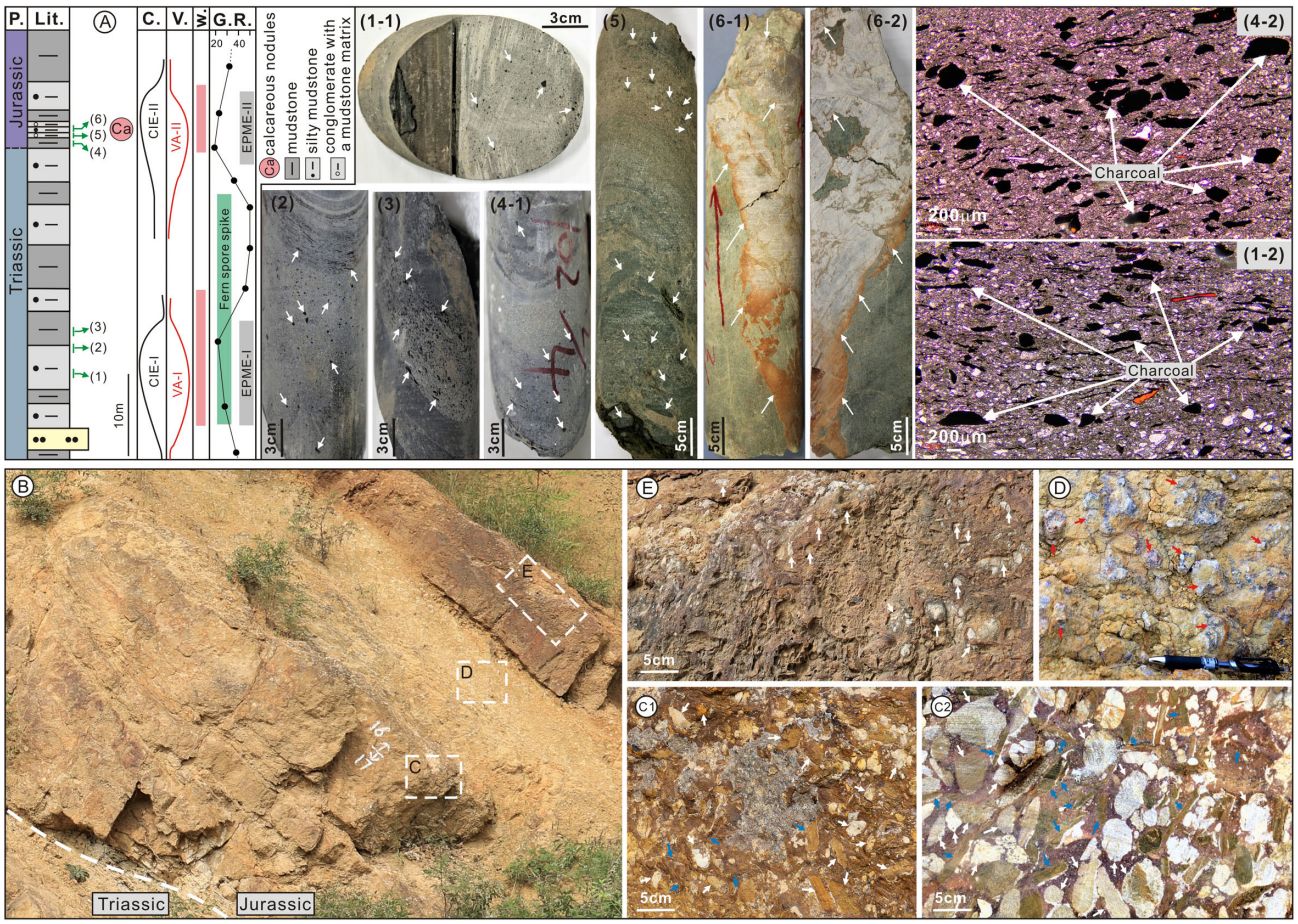

FIGURE 7 | Examples of abundant charcoal, conglomerate, mudstone clasts, and calcareous nodules from the borehole ZJ-1 and Sanhuang village section in the Jiyuan Basin during the Triassic-Jurassic transition. **(A)** Lithology, stratigraphic sequence, negative $\delta^{13}C_{org}$ excursions, volcanism, wildfire, and generic richness (number of difference genera) in the ZJ-1 borehole during the Triassic-Jurassic transition. Note (1-1), (2), (3), and (4-1) show abundant charcoal fossils in the middle Anyao Formation in the ZJ-1 borehole; (1-2) and (4-2) show microscopic images of charcoal fossils in the middle Anyao Formation in the ZJ-1 borehole; (5) shows mudstone clasts in the middle Anyao Formation in the ZJ-1 borehole; (6-1) and (6-2) show calcareous nodules in the middle Anyao Formation in the ZJ-1 borehole. **(B)** Lithology in the Sanhuang village section during the Triassic-Jurassic transition. **(C1,C2,D,E)** Abundant conglomerate, mudstone clasts, and calcareous nodules from the Sanhuang village section during the Triassic-Jurassic transition. Note the white arrows represent conglomerate, blue arrows represent mudstone clasts, red arrows represent calcareous nodules. P., Period; Lit., Lithology; C., Carbon cycle; V., Volcanism; W., Wildfire; G. R., Generic richness; CIE, carbon isotope excursion; VA, interval of volcanic activity; ETME-I, first phase to the second phase of the end-Triassic mass extinction; ETME-II, second phase to the second phase of the end-Triassic mass extinction.

to CAMP volcanism and its direct effects was responsible for the CIEs (e.g., Capriolo et al., 2021b), and drove contemporaneous global warming, as suggested by the PCA results.

Though global warming as a result of large-scale volcanism could be expected to have a major impact on plants, it appears that the development of intense wildfires—an indirect function of volcanism—seems to have the most profound impact on terrestrial plant ecosystems (**Figure 8** and **Supplementary Figure 6**). We suggest that the warming climate resulting from pulsed CAMP eruptions increased the frequency of lightning and wildfires (see **Supplementary Material**), resulting in the deterioration of terrestrial ecosystems (e.g., soil erosion) and associated reductions in plant diversity (**Figures 2**, **6**, **8** and **Supplementary Figure 6**). Frequent and intense wildfires were not only the direct cause of changes in terrestrial plant ecosystems and species diversity but also represent a vital link between the lake and terrestrial ecological crisis (e.g., Lu et al., 2020a; Mays et al., 2021). Thus, wildfire disruption to land surface vegetation would cause increased soil erosion, itself increasing nutrient runoff, but also further exposing bedrock and increasing continental weathering leading to siltation (Glasspool et al., 2015; Lu et al., 2020a). These processes can lead to large amounts of OM (including charcoal and un-charred material), and other substances entering the lake system through surface runoff (**Supplementary Figure 6**), promoting eutrophication and blooms of cyanobacteria and algae in freshwater environments, just as shown in the Jiyuan Basin. In this case, oxygen circulation between freshwater and atmosphere would have been inhibited by floating inert organic particles, cyanobacteria and algae in surface waters (e.g., Lu et al., 2020a). Cyanobacterial and algal

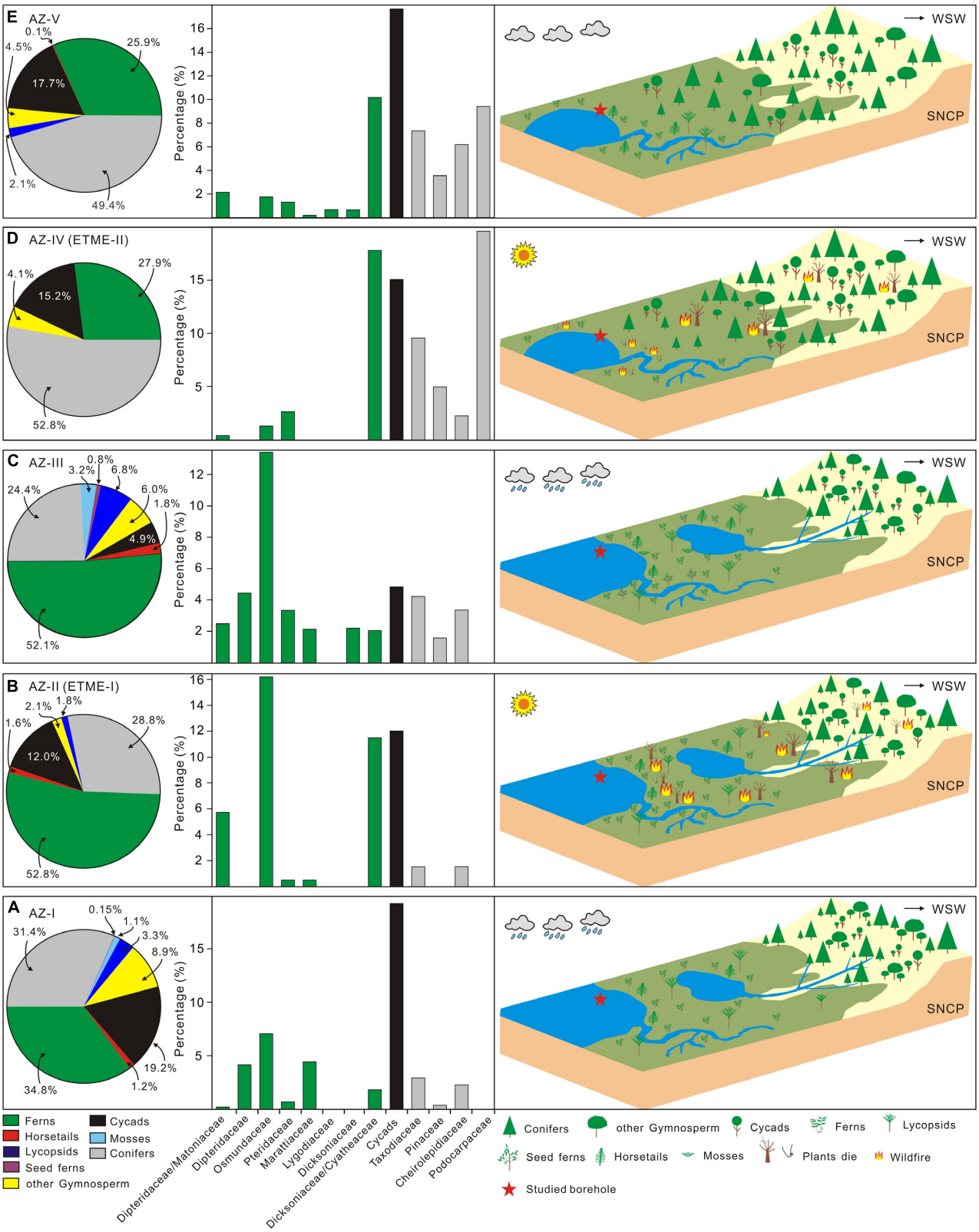

FIGURE 8 | Paleovegetation composition and paleoenvironmental reconstruction of the Jiyuan Basin illustrating five distinct **(A–E)** floral assemblages across the Triassic-Jurassic transition. AZ-I to AZ-V, palynology assemblage zone (AZ) I to the V; ETME-I, first stage of the end Triassic mass extinction; ETME-II, second stage of the end Triassic mass extinction; WSW, west-southwest; SNCP, southern North China Plate.

blooms would likely have contributed to the consumption of dissolved oxygen through decomposition post-mortem. It is possible that they produced secondary metabolites toxic to animals, impeding the recovery of lake freshwater ecosystems (Mays et al., 2021) in a scenario, similar to that proposed for the Carnian Pluvial Episode (Lu et al., 2021a) and the end-Permian extinction (Mays et al., 2021).

DATA AVAILABILITY STATEMENT

The original contributions presented in the study are included in the article/**Supplementary Material**, further inquiries can be directed to the corresponding author/s.

AUTHOR CONTRIBUTIONS

PZ, JL, MY, LS, and JH designed the research. JL, PZ, MY, LS, LL, and JH analyzed the data. PZ, JL, MY, LS, DB, SG, LL, and JH wrote the manuscript. All authors contributed to the interpretation of the data and to the final manuscript.

FUNDING

Financial support was provided from the National Key Research and Development Program of China (2021YFC2902000), the Natural Environment Research Council's Biosphere Evolution, Transition and Resilience (BETR) Program (NE/P0137224/1), the National Natural Science Foundation of China (Grant nos. 42172196, 41772161, and 41472131), and the National Science and Technology Major Project (Award no. 2017ZX05009-002).

ACKNOWLEDGMENTS

We are grateful to Suping Peng and Shifeng Dai (China University of Mining and Technology Beijing) for comments on earlier versions of the manuscript. We thank Simonetta Cirilli and Guillaume Paris for constructive and helpful reviews of the manuscript.

SUPPLEMENTARY MATERIAL

The Supplementary Material for this article can be found online at: https://www.frontiersin.org/articles/10.3389/fevo.2022.853404/full#supplementary-material

REFERENCES

Bacon, K. L., Belcher, C. M., Hesselbo, S. P., and McElwain, J. C. (2011). The Triassic-Jurassic boundary carbon-isotope excursions expressed in taxonomically identified leaf cuticles. *Palaios* 26, 461–469. doi: 10.2110/palo.2010.p10-120r

Barbacka, M., Pacyna, G., Kocsis, Á. T., Jarzynka, A., Ziaja, J., and Bodor, E. (2017). Changes in terrestrial floras at the Triassic-Jurassic Boundary in Europe. *Palaeogeogr. Palaeoclimatol. Palaeoecol.* 480, 80–93. doi: 10.1016/j.palaeo.2017.05.024

Bartolini, A., Guex, J., Spangenberg, J. E., Schoene, B., Taylor, D. G., Schaltegger, U., et al. (2012). Disentangling the Hettangian carbon isotope record: implications for the aftermath of the end-Triassic mass extinction. *Geochem. Geophys. Geosyst.* 13:Q01007. doi: 10.1029/2011GC003807

Belcher, C. M., Mander, L., Rein, G., Jervis, F. X., Haworth, M., Hesselbo, S. P., et al. (2010). Increased fire activity at the Triassic/Jurassic boundary in Greenland due to climate-driven floral change. *Nat. Geosci.* 3, 426–429. doi: 10.1038/ngeo871

Bond, D. P. G., and Wignall, P. B. (2014). "Large igneous provinces and mass extinctions: an update," in *Volcanism, Impacts, and Mass Extinctions: Causes and Effects*, eds G. Keller and A. C. Kerr (Boulder, CO: Geological Society of America), 29–55.

Bonis, N. R., Kürschner, W. M., and Krystyn, L. (2009). A detailed palynological study of the Triassic-Jurassic transition in key sections of the Eiberg Basin (Northern Calcareous Alps, Austria). *Rev. Palaeobot. Palynol.* 156, 376–400. doi: 10.1016/j.revpalbo.2009.04.003

Bonis, N. R., Ruhl, M., and Kürschner, W. M. (2010). Milankovitch-scale palynological turnover across the Triassic-Jurassic transition at St. Audrie's Bay, SW UK. *J. Geol. Soc. Lond.* 167, 877–888. doi: 10.1144/0016-76492009-141

Boomer, I., Copestake, P., Raine, R., Azmi, A., Fenton, J. P. G., Page, K. N., et al. (2021). Stratigraphy, palaeoenvironments and geochemistry across the Triassic-Jurassic boundary transition at Carnduff, County Antrim, Northern Ireland. *Proc. Geol. Assoc.* 132, 667–687. doi: 10.1016/j.pgeola.2020.05.004

Bustin, R., and Guo, Y. (1999). Abrupt changes (jumps) in reflectance values and chemical compositions of artificial charcoals and inertinite in coals. *Int. J. Coal Geol.* 38, 237–260. doi: 10.1016/S0166-5162(98)00025-1

Capriolo, M., Marzoli, A., Aradi, L. E., Ackerson, M. R., Bartoli, O., Callegaro, S., et al. (2021a). Massive methane fluxing from magma–sediment interaction in the end-Triassic Central Atlantic Magmatic Province. *Nat. Commun.* 12:5534. doi: 10.1038/s41467-021-25510-w

Capriolo, M., Mills, B. J. W., Newton, R. J., Corso, J. D., Dunhill, A. M., Wignall, P. B., et al. (2021b). Anthropogenic-scale CO_2 degassing from the Central Atlantic Magmatic Province as a driver of the end-Triassic mass extinction. *Glob. Planet. Change* 209:103731. doi: 10.1016/j.gloplacha.2021.103731

Cirilli, S. (2010). Upper Triassic-lowermost Jurassic palynology and palynostratigraphy: a review. *Geol. Soc. Spec. Publ.* 334, 285–314. doi: 10.1144/SP334.12

Cirilli, S., Buratti, N., Gugliotti, L., and Frixa, A. (2015). Palynostratigraphy and palynofacies of the Upper Triassic Streppenosa Formation (SE Sicily, Italy) and inference on the main controlling factors in the organic rich shale deposition. *Rev. Palaeobot. Palynol.* 218, 67–79. doi: 10.1016/j.revpalbo.2014.10.009

Cirilli, S., Marzoli, A., Tanner, L., Bertrand, H., Buratti, N., Jourdan, F., et al. (2009). Latest Triassic onset of the Central Atlantic Magmatic Province (CAMP) volcanism in the Fundy Basin (Nova Scotia): new stratigraphic constraints. *Earth Planet. Sci. Lett.* 286, 514–525. doi: 10.1016/j.epsl.2009.07.021

Cirilli, S., Panfili, G., Buratti, N., and Frixa, A. (2018). Paleoenvironmental reconstruction by means of palynofacies and lithofacies analyses: an example from the Upper Triassic subsurface succession of the Hyblean Plateau Petroleum System (SE Sicily, Italy). *Rev. Palaeobot. Palynol.* 253, 70–87. doi: 10.1016/j.revpalbo.2018.04.003

Clémence, M., Bartolini, A., Gardin, S., Paris, G., Beaumont, V., and Page, K. N. (2010). Early Hettangian benthic–planktonic coupling at Doniford (SW England). *Palaeogeogr. Palaeoclimatol. Palaeoecol.* 295, 102–115. doi: 10.1016/j.palaeo.2010.05.021

Cloern, J. E., Canuel, E. A., and Harris, D. (2002). Stable carbon and nitrogen isotope composition of aquatic and terrestrial plants of the San Francisco Bay estuarine system. *Limnol. Oceanogr.* 47, 713–729. doi: 10.4319/lo.2002.47.3.0713

Collister, J. W., Rieley, G., Stern, B., Eglinton, G., and Fry, B. (1994). Compound-specific δ13C analyses of leaf lipids from plants with differing carbon dioxide metabolisms. *Org. Geochem.* 21, 619–627. doi: 10.1016/0146-6380(94)90008-6

Dal Corso, J., Gianolla, P., Rigo, M., Franceschi, M., Roghi, G., Mietto, P., et al. (2018). Multiple negative carbon-isotope excursions during the Carnian Pluvial Episode (Late Triassic). *Earth Sci. Rev.* 185, 732–750. doi: 10.1016/j.earscirev.2018.07.004

Dal Corso, J., Marzoli, A., Tateo, F., Jenkyns, H. C., Bertrand, H., Youbi, N., et al. (2014). The dawn of CAMP volcanism and its bearing on the end-Triassic carbon cycle disruption. *J. Geol. Soc. Lond.* 171, 153–164. doi: 10.1144/jgs2013-063

Dal Corso, J., Song, H. J., Callegaro, S., Chu, D. L., Sun, Y. D., Hilton, J., et al. (2022). Environmental crises at the Permian–Triassic mass extinction. *Nat. Rev. Earth Environ.* doi: 10.1038/s43017-021-00259-4

De Jersey, N. J., and McKellar, J. L. (2013). The palynology of the Triassic-Jurassic transition in southeastern Queensland, Australia, and correlation with New Zealand. *Palynology* 37, 77–114. doi: 10.1080/01916122.2012.718609

Deng, S. H., Lu, Y. Z., Fan, R., Pan, Y. H., Cheng, X. S., Fu, G. B., et al. (2010). *The Jurassic System of Northern Xinjiang, China*. Hefei: University of Science and Technology of China Press. (in Chinese with English abstract).

Diefendorf, A. F., and Freimuth, E. J. (2017). Extracting the most from terrestrial plant-derived n-alkyl lipids and their carbon isotopes from the sedimentary record: a review. *Org. Geochem.* 103, 1–21. doi: 10.1016/j.orggeochem.2016.10.016

Fang, Y., Fang, L., Deng, S., Lu, Y., Wang, B., Zhao, X., et al. (2021). Carbon isotope stratigraphy across the Triassic-Jurassic boundary in the high-latitude terrestrial Junggar Basin, NW China. *Palaeogeogr. Palaeoclimatol. Palaeoecol.* 577:110559. doi: 10.1016/j.palaeo.2021.110559

Fu, Z., and Yuan, X. (1998). Late Triassic sporopollen assemblage from Liupanshan Basin of Ningxia and their stratigraphical significance. *Acta Palaeontol. Sin.* 37, 446–454.

Glasspool, I. J., Scott, A. C., Waltham, D., Pronina, N., and Shao, L. (2015). The impact of fire on the late Paleozoic Earth System. *Front. Plant Sci.* 6:756. doi: 10.3389/fpls.2015.00756

Goodarzi, F. (1985). Optically anisotropic fragments in a Western Canadian subbituminous coal. *Fuel* 64, 1294–1300. doi: 10.1016/0016-2361(85)90191-7

Greene, S. E., Martindale, R. C., Ritterbush, K. A., Bottjer, D. J., Corsetti, F. A., and Berelson, W. M. (2012). Recognising ocean acidification in deep time: an evaluation of the evidence for acidification across the Triassic-Jurassic boundary. *Earth Sci. Rev.* 113, 72–93. doi: 10.1016/j.earscirev.2012.03.009

Heimdal, T. H., Jones, M. T., and Henrik, H. S. (2020). Thermogenic carbon release from the Central Atlantic magmatic province caused major end-Triassic carbon cycle perturbations. *Proc. Natl. Acad. Sci. U.S.A.* 117, 11968–11974. doi: 10.1073/pnas.2000095117

Heimdal, T. H., Svensen, H. H., Ramezani, J., Iyer, K., Pereira, E., Rodrigues, R., et al. (2018). Large-scale sill emplacement in Brazil as a trigger for the end-Triassic crisis. *Sci. Rep.* 8:141. doi: 10.1038/s41598-017-18629-8

Hesselbo, S. P., Robinson, S. A., Surlyk, F., and Piasecki, S. (2002). Terrestrial and marine extinction at the Triassic-Jurassic boundary synchronized with major carbon-cycle perturbation: a link to initiation of massive volcanism? *Geology* 30, 251–254. doi: 10.1130/0091-7613(2002)030<0251:tameat>2.0.co;2

Hu, B. (1991). The late Triassic and middle Jurassic continental strata in Jiyuan basin, Henan Province. *J. Stratigr.* 15, 48–52.

Huang, Q. (2001). Early Jurassic flora and paleoenvironment in Daxian and Kaixian counties, northern border of Sichuan basin (in Chinese with English abstract). *Earth Sci. China Univ. Geosci.* 26, 221–227.

Ivany, L. C., and Salawitch, R. J. (1993). Carbon isotopic evidence for biomass burning at the K-T boundary. *Geology* 21:487. doi: 10.1130/0091-7613(1993)021<0487:ciefbb>2.3.co;2

Jones, T. P., Ash, S., and Figueiral, I. (2002). Late Triassic charcoal from Petrified Forest National Park, Arizona, USA. *Palaeogeogr. Palaeoclimatol. Palaeoecol.* 188, 127–139. doi: 10.1016/S0031-0182(02)00549-7

Korte, C., Hesselbo, S. P., Jenkyns, H. C., Rickaby, R. E. M., and Spötl, C. (2009). Palaeoenvironmental significance of carbon- and oxygen-isotope stratigraphy of marine Triassic–Jurassic boundary sections in SW Britain. *J. Geol. Soc. Lond.* 166, 431–445. doi: 10.1144/0016-76492007-177

Korte, C., Ruhl, M., Pálfy, J., Ullmann, C. V., and Hesselbo, S. P. (2019). "Chemostratigraphy across the Triassic-Jurassic boundary," in *Chemostratigraphy Across Major Chronological Boundaries*, eds A. N. Sial, C. Gaucher, M. Ramkumar, and V. P. Ferreira (Washington, DC: American Geophysical Union (AGU)), 183–210. doi: 10.1002/9781119382508.ch10

Kovács, E. B., Ruhl, M., Demény, A., Fórizs, I., Hegyi, I., Horváth-Kostka, Z. R., et al. (2020). Mercury anomalies and carbon isotope excursions in the western Tethyan Csővár section support the link between CAMP volcanism and the end-Triassic extinction. *Glob. Planet. Change* 194:103291. doi: 10.1016/j.gloplacha.2020.103291

Kuerschner, W. M., Bonis, N. R., and Krystyn, L. (2007). Carbon-isotope stratigraphy and palynostratigraphy of the Triassic–Jurassic transition in the Tiefengraben section – Northern Calcareous Alps (Austria). *Palaeogeogr. Palaeoclimatol. Palaeoecol.* 244, 257–280. doi: 10.1016/j.palaeo.2006.06.031

Landwehrs, J. P., Feulner, G., Hofmann, M., and Petri, S. (2020). Climatic fluctuations modeled for carbon and sulfur emissions from end-Triassic volcanism. *Earth Planet. Sci. Lett.* 537:116174. doi: 10.1016/j.epsl.2020.116174

Li, L., Wang, Y., Kürschner, W. M., Ruhl, M., and Vajda, V. (2020). Palaeovegetation and palaeoclimate changes across the Triassic – Jurassic transition in the Sichuan Basin, China. *Palaeogeogr. Palaeoclimatol. Palaeoecol.* 556:109891. doi: 10.1016/j.palaeo.2020.109891

Li, M., Zheng, D., Dai, G., Liu, C., and Zhou, L. (2014). Geochemical characteristics of the Jurassic argillaceous rocks of the Jiyuan Basin, Western Henan and the implications for environments and provenances. *Acta Geol. Sin.* 88, 229–238.

Lindström, S. (2016). Palynofloral patterns of terrestrial ecosystem change during the end-Triassic event – a review. *Geol. Mag.* 153, 223–251. doi: 10.1017/S0016756815000552

Lindström, S. (2021). Two-phased mass rarity and extinction in land plants during the end-Triassic climate crisis. *Front. Earth Sci.* 9:780343. doi: 10.3389/feart.2021.780343

Lindström, S., Callegaro, S., Davies, J., Tegner, C., van de Schootbrugge, B., Pedersen, G. K., et al. (2021). Tracing volcanic emissions from the Central Atlantic Magmatic Province in the sedimentary record. *Earth Sci. Rev.* 212:103444. doi: 10.1016/j.earscirev.2020.103444

Lindström, S., Sanei, H., van de Schootbrugge, B., Pedersen, G. K., Lesher, C. E., Tegner, C., et al. (2019). Volcanic mercury and mutagenesis in land plants during the end-Triassic mass extinction. *Sci. Adv.* 5:eaaw4018. doi: 10.1126/sciadv.aaw4018

Lindström, S., van de Schootbrugge, B., Hansen, K. H., Pedersen, G. K., Alsen, P., Thibault, N., et al. (2017). A new correlation of Triassic–Jurassic boundary successions in NW Europe, Nevada and Peru, and the Central Atlantic Magmatic Province: a time-line for the end-Triassic mass extinction. *Palaeogeogr. Palaeoclimatol. Palaeoecol.* 478, 80–102. doi: 10.1016/j.palaeo.2016.12.025

Liu, S., Su, S., and Zhang, G. (2013). Early Mesozoic basin development in North China: indications of cratonic deformation. *J. Asian Earth Sci.* 62, 221–236. doi: 10.1016/j.jseaes.2012.09.011

Liu, Z., Li, L., and Wang, Y. (2015). Late Triassic spore-pollen assemblage from Xuanhan of Sichuan,China. *Acta Micropala Eontol. Sin.* 32, 43–62. doi: 10.16087/j.cnki.1000-0674.20150407.006

Lu, J., Zhang, P., Dal Corso, J., Yang, M., Wignall, P. B., Greene, S. E., et al. (2021a). Volcanically driven lacustrine ecosystem changes during the Carnian Pluvial Episode (Late Triassic). *Proc. Natl. Acad. Sci. U.S.A.* 118:e2109895118. doi: 10.1073/pnas.2109895118

Lu, J., Zhou, K., Yang, M., Zhang, P., Shao, L., and Hilton, J. (2021b). Records of organic carbon isotopic composition ($\delta^{13}C_{org}$) and volcanism linked to changes in atmospheric pCO_2 and climate during the Late Paleozoic Icehouse. *Glob. Planet. Change* 207:103654. doi: 10.1016/j.gloplacha.2021.103654

Lu, J., Wang, Y., Yang, M., Shao, L., and Hilton, J. (2021c). Records of volcanism and organic carbon isotopic composition ($\delta^{13}C_{org}$) linked to changes in atmospheric pCO_2 and climate during the Pennsylvanian icehouse interval. *Chem. Geol.* 570:120168. doi: 10.1016/j.chemgeo.2021.120168

Lu, J., Zhang, P., Yang, M., Shao, L., and Hilton, J. (2020a). Continental records of organic carbon isotopic composition ($\delta^{13}C_{org}$), weathering, paleoclimate and wildfire linked to the End-Permian Mass Extinction. *Chem. Geol.* 558:119764. doi: 10.1016/j.chemgeo.2020.119764

Lu, J., Zhou, K., Yang, M., Eley, Y., Shao, L., and Hilton, J. (2020b). Terrestrial organic carbon isotopic composition ($\delta^{13}C_{org}$) and environmental

perturbations linked to Early Jurassic volcanism: evidence from the Qinghai-Tibet Plateau of China. *Glob. Planet. Change* 195:103331. doi: 10.1016/j.gloplacha.2020.103331

Lu, Y., and Deng, S. (2005). Triassic-Jurassic sporopollen assemblages on the Southern Margin of the Junggar Basin, Xinjiang and the T-J Boundary. *Acta Geol. Sin.* 1, 15–28. doi: 10.3321/j.issn:0001-5717.2005.01.003

Lucas, S. G. (2021). "End-triassic extinctions," in *Encyclopedia of Geology*, eds D. Alderton and S. A. Elias (Amsterdam: Elsevier), 653–664. doi: 10.1016/B978-0-12-409548-9.12013-5

Lucas, S. G., and Tanner, L. H. (2015). End-Triassic nonmarine biotic events. *J. Palaeogeogr.* 4, 331–348. doi: 10.1016/j.jop.2015.08.010

Marynowski, L., and Simoneit, B. R. T. (2009). Widespread upper Triassic to lower Jurassic wildfire records from poland: evidence from charcoal and pyrolytic polycyclic aromatic hydrocarbons. *Palaios* 24, 785–798. doi: 10.2110/palo.2009.p09-044r

Marzoli, A., Bertrand, H., Knight, K. B., Cirilli, S., Buratti, N., Vérati, C., et al. (2004). Synchrony of the Central Atlantic magmatic province and the Triassic-Jurassic boundary climatic and biotic crisis. *Geology* 32, 973–976. doi: 10.1130/G20652.1

Marzoli, A., Bertrand, H., Knight, K. B., Cirilli, S., Nomade, S., Renne, P. R., et al. (2008). Comment on "Synchrony between the Central Atlantic magmatic province and the Triassic-Jurassic mass-extinction event? By Whiteside et al. (2007)." *Palaeogeogr. Palaeoclimatol. Palaeoecol.* 262, 189–193. doi: 10.1016/j.palaeo.2008.01.016

Mays, C., McLoughlin, S., Frank, T. D., Fielding, C. R., Slater, S. M., and Vajda, V. (2021). Lethal microbial blooms delayed freshwater ecosystem recovery following the end-Permian extinction. *Nat. Commun.* 12:5511. doi: 10.1038/s41467-021-25711-3

McElwain, J. C., Beerling, D. J., and Woodward, F. I. (1999). Fossil plants and global warming at the Triassic-Jurassic boundary. *Science* 285, 1386–1390. doi: 10.1126/science.285.5432.1386

McElwain, J. C., Popa, M. E., Hesselbo, S. P., Haworth, M., and Surlyk, F. (2007). Macroecological responses of terrestrial vegetation to climatic and atmospheric change across the Triassic/Jurassic boundary in East Greenland. *Paleobiology* 33, 547–573. doi: 10.1666/06026.1

Miller, C. S., and Baranyi, V. (2021). "Triassic climates," in *Encyclopedia of Geology*, eds D. Alderton and S. A. B. T. Elias (Oxford: Elsevier), 514–524. doi: 10.1016/B978-0-12-409548-9.12070-6

Olsen, P. E., Kent, D. V., Sues, H. D., Koeberl, C., Huber, H., Montanari, A., et al. (2002). Ascent of dinosaurs linked to an iridium anomaly at the Triassic-Jurassic boundary. *Science* 296, 1305–1307. doi: 10.1126/science.1065522

Panfili, G., Cirilli, S., Corso, J. D., Bertrand, H., Medina, F., Youbi, N., et al. (2019). New biostratigraphic constraints show rapid emplacement of the Central Atlantic Magmatic Province (CAMP) during the end-Triassic mass extinction interval. *Glob. Planet. Change* 172, 60–68. doi: 10.1016/j.gloplacha.2018.09.009

Paris, G., Donnadieu, Y., Beaumont, V., Fluteau, F., and Goddéris, Y. (2016). Geochemical consequences of intense pulse-like degassing during the onset of the Central Atlantic Magmatic Province. *Palaeogeogr. Palaeoclimatol. Palaeoecol.* 441, 74–82. doi: 10.1016/j.palaeo.2015.04.011

Percival, L. M. E., Ruhl, M., Hesselbo, S. P., Jenkyns, H. C., Mather, T. A., and Whiteside, J. H. (2017). Mercury evidence for pulsed volcanism during the end-Triassic mass extinction. *Proc. Natl. Acad. Sci. U.S.A.* 114, 7929–7934. doi: 10.1073/pnas.1705378114

Petersen, H. I., and Lindström, S. (2012). Synchronous wildfire activity rise and mire deforestation at the Triassic–Jurassic boundary. *PLoS One* 7:e47236. doi: 10.1371/journal.pone.0047236

Pieńkowski, G., Hesselbo, S. P., Barbacka, M., and Leng, M. J. (2020). Non-marine carbon-isotope stratigraphy of the Triassic-Jurassic transition in the Polish Basin and its relationships to organic carbon preservation, pCO_2 and palaeotemperature. *Earth Sci. Rev.* 210:103383. doi: 10.1016/j.earscirev.2020.103383

Pieńkowski, G., Niedźwiedzki, G., and Waksmundzka, M. (2012). Sedimentological, palynological and geochemical studies of the terrestrial Triassic-Jurassic boundary in northwestern Poland. *Geol. Mag.* 149, 308–332. doi: 10.1017/S0016756811000914

Raup, D. M., and Sepkoski, J. J. (1982). Mass extinctions in the marine fossil record. *Science* 215, 1501–1503. doi: 10.1126/science.215.4539.1501

Ruhl, M., Deenen, M. H. L., Abels, H. A., Bonis, N. R., Krijgsman, W., and Kürschner, W. M. (2010). Astronomical constraints on the duration of the early Jurassic Hettangian stage and recovery rates following the end-Triassic mass extinction (St Audrie's Bay/East Quantoxhead, UK). *Earth Planet. Sci. Lett.* 295, 262–276. doi: 10.1016/j.epsl.2010.04.008

Ruhl, M., Hesselbo, S. P., Al-Suwaidi, A., Jenkyns, H. C., Damborenea, S. E., Manceñido, M. O., et al. (2020). On the onset of Central Atlantic Magmatic Province (CAMP) volcanism and environmental and carbon-cycle change at the Triassic–Jurassic transition (Neuquén Basin, Argentina). *Earth Sci. Rev.* 208:103229. doi: 10.1016/j.earscirev.2020.103229

Ruhl, M., Kürschner, W. M., and Krystyn, L. (2009). Triassic–Jurassic organic carbon isotope stratigraphy of key sections in the western Tethys realm (Austria). *Earth Planet. Sci. Lett.* 281, 169–187. doi: 10.1016/j.epsl.2009.02.020

Schaller, M. F., Wright, J. D., and Kent, D. V. (2011). Atmospheric PCO_2 perturbations associated with the central Atlantic magmatic province. *Science* 331, 1404–1409. doi: 10.1126/science.1199011

Schaltegger, U., Guex, J., Bartolini, A., Schoene, B., and Ovtcharova, M. (2008). Precise U-Pb age constraints for end-Triassic mass extinction, its correlation to volcanism and Hettangian post-extinction recovery. *Earth Planet. Sci. Lett.* 267, 266–275. doi: 10.1016/j.epsl.2007.11.031

Schoene, B., Guex, J., Bartolini, A., Schaltegger, U., and Blackburn, T. J. (2010). Correlating the end-Triassic mass extinction and flood basalt volcanism at the 100 ka level. *Geology* 38, 387–390. doi: 10.1130/G30683.1

Sha, J., Olsen, P. E., Pan, Y., Xu, D., Wang, Y., Zhang, X., et al. (2015). Triassic–Jurassic climate in continental high-latitude Asia was dominated by obliquity-paced variations (Junggar Basin, Ürümqi, China). *Proc. Natl. Acad. Sci. U.S.A.* 112, 3624–3629. doi: 10.1073/pnas.1501137112

Shen, J., Feng, Q., Algeo, T. J., Liu, J., Zhou, C., Wei, W., et al. (2020). Sedimentary host phases of mercury (Hg) and implications for use of Hg as a volcanic proxy. *Earth Planet. Sci. Lett.* 543:116333. doi: 10.1016/j.epsl.2020.116333

Shen, J., Yin, R., Zhang, S., Algeo, T. J., Bottjer, D. J., Yu, J., et al. (2022). Intensified continental chemical weathering and carbon-cycle perturbations linked to volcanism during the Triassic–Jurassic transition. *Nat. Commun.* 13:299. doi: 10.1038/s41467-022-27965-x

Slodownik, M., Vajda, V., and Steinthorsdottir, M. (2021). Fossil seed fern *Lepidopteris ottonis* from Sweden records increasing CO_2 concentration during the end-Triassic extinction event. *Palaeogeogr. Palaeoclimatol. Palaeoecol.* 564:110157. doi: 10.1016/j.palaeo.2020.110157

Song, Y., Algeo, T. J., Wu, W., Luo, G., Li, L., Wang, Y., et al. (2020). Distribution of pyrolytic PAHs across the Triassic-Jurassic boundary in the Sichuan Basin, southwestern China: evidence of wildfire outside the Central Atlantic Magmatic Province. *Earth Sci. Rev.* 201:102970. doi: 10.1016/j.earscirev.2019.102970

Srivastava, S. K. (1976). The fossil pollen genus *Classopollis*. *Lethaia* 9, 437–457. doi: 10.1111/j.1502-3931.1976.tb00985.x

Steinthorsdottir, M., Jeram, A. J., and McElwain, J. C. (2011). Extremely elevated CO_2 concentrations at the Triassic/Jurassic boundary. *Palaeogeogr. Palaeoclimatol. Palaeoecol.* 308, 418–432. doi: 10.1016/j.palaeo.2011.05.050

Svensen, H., Planke, S., Polozov, A. G., Schmidbauer, N., Corfu, F., Podladchikov, Y. Y., et al. (2009). Siberian gas venting and the end-Permian environmental crisis. *Earth Planet. Sci. Lett.* 277, 490–500. doi: 10.1016/j.epsl.2008.11.015

Thibodeau, A. M., Ritterbush, K., Yager, J. A., West, A. J., Ibarra, Y., Bottjer, D. J., et al. (2016). Mercury anomalies and the timing of biotic recovery following the end-Triassic mass extinction. *Nat. Commun.* 7:11147. doi: 10.1038/ncomms11147

Vajda, V., Calner, M., and Ahlberg, A. (2013). Palynostratigraphy of dinosaur footprint-bearing deposits from the Triassic-Jurassic boundary interval of Sweden. *GFF* 135, 120–130. doi: 10.1080/11035897.2013.799223

van de Schootbrugge, B., Payne, J. L., Tomasovych, A., Pross, J., Fiebig, J., Benbrahim, M., et al. (2008). Carbon cycle perturbation and stabilization in the wake of the Triassic-Jurassic boundary mass-extinction event. *Geochem. Geophys. Geosyst.* 9:Q04028. doi: 10.1029/2007GC001914

van de Schootbrugge, B., Quan, T. M., Lindström, S., Püttmann, W., Heunisch, C., Pross, J., et al. (2009). Floral changes across the Triassic/Jurassic boundary linked to flood basalt volcanism. *Nat. Geosci.* 2, 589–594. doi: 10.1038/ngeo577

van de Schootbrugge, B., van der Weijst, C. M. H., Hollaar, T. P., Vecoli, M., Strother, P. K., Kuhlmann, N., et al. (2020). Catastrophic soil loss associated

with end-Triassic deforestation. *Earth Sci. Rev.* 210:103332. doi: 10.1016/j.earscirev.2020.103332

Vervoort, P., Adloff, M., Greene, S. E., and Kirtland Turner, S. (2019). Negative carbon isotope excursions: an interpretive framework. *Environ. Res. Lett.* 14:085014. doi: 10.1088/1748-9326/ab3318

Vilas-Boas, M., Pereira, Z., Cirilli, S., Duarte, L. V., and Fernandes, P. (2021). New data on the palynology of the Triassic–Jurassic boundary of the Silves Group, Lusitanian Basin, Portugal. *Rev. Palaeobot. Palynol.* 290:104426. doi: 10.1016/j.revpalbo.2021.104426

Wang, Y. D., Fu, B. H., Xie, X. P., Huang, Q. S., Li, K., Li, G., et al. (2010). *The Terrestrial Triassic and Jurassic Systems in the Sichuan Basin, China*. Hefei: University of Science and Technology of China Press, 1–216. (in Chinese with English abstract).

Whiteside, J. H., Olsen, P. E., Kent, D. V., Fowell, S. J., and Et-Touhami, M. (2007). Synchrony between the Central Atlantic magmatic province and the Triassic–Jurassic mass-extinction event? *Palaeogeogr. Palaeoclimatol. Palaeoecol.* 244, 345–367. doi: 10.1016/j.palaeo.2006.06.035

Wignall, P. B., and Atkinson, J. W. (2020). A two-phase end-Triassic mass extinction. *Earth Sci. Rev.* 208:103282. doi: 10.1016/j.earscirev.2020.103282

Wotzlaw, J. F., Guex, J., Bartolini, A., Gallet, Y., Krystyn, L., McRoberts, C. A., et al. (2014). Towards accurate numerical calibration of the Late Triassic: high-precision U-Pb geochronology constraints on the duration of the Rhaetian. *Geology* 42, 571–574. doi: 10.1130/G35612.1

Yager, J. A., West, A. J., Thibodeau, A. M., Corsetti, F. A., Rigo, M., Berelson, W. M., et al. (2021). Mercury contents and isotope ratios from diverse depositional environments across the Triassic–Jurassic Boundary: towards a more robust mercury proxy for large igneous province Magmatism. *Earth Sci. Rev.* 223:103775. doi: 10.1016/j.earscirev.2021.103775

Yang, W., Yang, J., Wang, X., and Du, Y. (2012). Geochronology from Middle Triassic to Middle Jurassic detrital zircons in Jiyuan basin and its implications for the Qinling Orogen. *Earth Sci. China Univ. Geosci.* 37, 489–500. doi: 10.3799/dqkx.2012.055

Zaffani, M., Jadoul, F., and Rigo, M. (2018). A new Rhaetian $\delta^{13}C_{org}$ record: carbon cycle disturbances, volcanism, End-Triassic mass Extinction (ETE). *Earth Sci. Rev.* 178, 92–104. doi: 10.1016/j.earscirev.2018.01.004

Zhou, N., Xu, Y., Li, L., Lu, N., An, P., Popa, M. E., et al. (2021). Pattern of vegetation turnover during the end-Triassic mass extinction: trends of fern communities from South China with global context. *Glob. Planet. Change* 205:103585. doi: 10.1016/j.gloplacha.2021.103585

Conflict of Interest: MY was employed by the company PetroChina.

The remaining authors declare that the research was conducted in the absence of any commercial or financial relationships that could be construed as a potential conflict of interest.

Publisher's Note: All claims expressed in this article are solely those of the authors and do not necessarily represent those of their affiliated organizations, or those of the publisher, the editors and the reviewers. Any product that may be evaluated in this article, or claim that may be made by its manufacturer, is not guaranteed or endorsed by the publisher.